Acta Materialia 296 (2025) 121272

Contents lists available at ScienceDirect

Acta Materialia

journal homepage: www.elsevier.com/locate/actamat

Full length article

Tribo-induced microstructural evolutions and wear mechanisms of $AlCoCrFeNi_{2.1}$ eutectic high-entropy alloy at elevated temperatures

Wei Jiang [a,*], Jian Zhou [a], Yang Cao [b,*], Ao Meng [a], Runchang Liu [c], Jiansheng Li [a], Zhumin Li [a], Yu Zhao [a,d], Yonghao Zhao [b,c,*]

[a] School of Materials Science and Engineering, Anhui Polytechnic University, Wuhu 241000, PR China
[b] School of Materials Science and Engineering, Hohai University, Changzhou 213200, PR China
[c] Nano and Heterogeneous Materials Center, School of Materials Science and Engineering, Nanjing University of Science and Technology, Nanjing 210094, PR China
[d] Key Laboratory of Additive Manufacturing (3D Printing) of Anhui Province, Anhui Polytechnic University, Wuhu 241000, PR China

ARTICLE INFO

Key words:
Eutectic high-entropy alloy
Friction and wear
High temperature
Oxidation

ABSTRACT

The tribological behaviors and wear mechanisms of the $AlCoCrFeNi_{2.1}$ eutectic high-entropy alloy (EHEA) were investigated in the broad temperature range 25 – 800 °C. The $AlCoCrFeNi_{2.1}$ EHEA exhibits a very low wear rate at 25 °C, owing to the formation of the composite type oxidation layer consisting of nanocrystals embedded in amorphous matrix. The EHEA exhibits decreasing trends for COF and stable wear rates with increasing temperature. The synergistic effect of oxidation and plastic deformation causes the formation and thickening of oxidation layer which is beneficial to wear resistance at 400 °C. At 800 °C, the high temperature enhances atomic diffusion, thus the amorphous oxide layer undergoes partial crystallization to form nano and ultrafine grains. Both the newly formed nanograins and ultrafine grains are thermally stable, and possess high hardness which can improve anti-wear performance of the alloy. This work gets insights into developing new wear-resistant alloys that is applicable in a broad temperature range, by revealing the tribo-induced surface deformation mechanisms.

1. Introduction

Since 2004, the emergence of high-entropy alloys (HEAs) has broadened the horizon for materials design [1–4]. The increasing number of studies has explored the superior properties of HEAs, especially the excellent synergy in strength-ductility [5,6], outstanding fracture toughness [7,8], exceptional resistance to creep [9,10] and remarkable work hardening ability [11,12], even across a wide temperature range. Recently, considerable interest has been attracted to the tribological behavior and wear mechanisms of HEAs, in seeking novel wear-resistant materials for engineering application [13,14]. The CoCrFeMnNi HEA and its variants, such as CoCrFeNi HEA and CrCoNi medium-entropy alloy (MEA) [14–18], are representative multi-principal element alloys (MPEA) with single-phase face-centered cubic (FCC) structures. These MPEAs in homogeneous coarse-grained states show excellent ductility, but low strength and poor wear resistance. Simple grain refinement to ultrafine grained and nanocrystalline regimes can significantly improve the strength of the FCC MPEAs, but their wear resistance was barely improved. This is because homogeneous nanocrystalline structures under sliding friction induced by shear deformation show brittle fracture, strain localization, surface roughening and cracks [19]. Constructing gradient nanostructures is proven a successful strategy to improve the wear resistance; because gradient nanostructures can inhibit inhomogeneous plastic deformation, and thus suppress sliding-induced cracks and local brittle fracture [19]. Alloying MPEAs with Mo [20], W [21], Al [22] and Nb [23], etc, to enhance solid solution or precipitation strengthening effects is another strategy to improve the wear resistance. For example, alloying the original single phase CoCrNi MEA with Nb additions, can form lamellar eutectic structure composed of FCC and Laves phases which can effectively prevent crack initiation and propagation, leading to lowered coefficients of friction (COF) and wear rates [24]. Similarly, the addition of Al into the body-centered cubic (BCC) structure TiZrNbHf refractory HEA results in severe lattice distortions that in turn enhances the strength and wear resistance [25].

Eutectic high-entropy alloys (EHEAs) are unique class of HEAs, featuring dual phase lamellar structures delineated by low-energy phase boundaries [26–28]. While the different phases on either side of the

* Corresponding authors.
E-mail addresses: JiangWei@ahpu.edu.cn (W. Jiang), y.cao@hhu.edu.cn (Y. Cao), yhzhao@njust.edu.cn (Y. Zhao).

https://doi.org/10.1016/j.actamat.2025.121272
Received 12 May 2025; Received in revised form 17 June 2025; Accepted 18 June 2025
Available online 18 June 2025

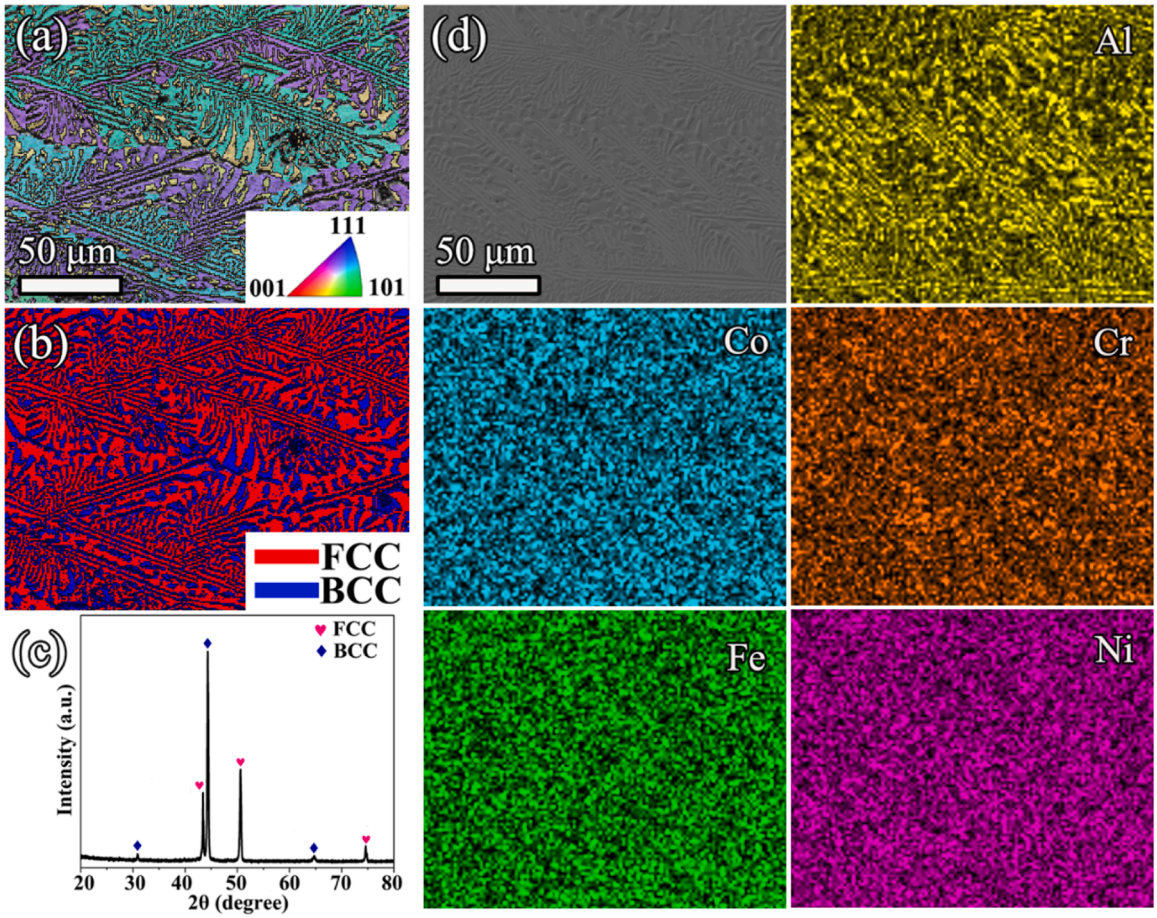

Fig 1. Microstructures and compositional distributions in the as-cast $AlCoCrFeNi_{2.1}$ EHEA: (a) an OIM image and the inset of the inverse pole figure color code; (b) a phase map; (c) the XRD pattern; (d) a set of SEM-EDS maps.

phase boundaries have distinguishable crystal structures and mechanical properties, the phase boundaries become the heterogeneous interfaces for which the stress and strain gradients can build-up upon them. The microscopic stress and strain gradients stimulate hetero-deformation induced (HDI) strengthening effect that contributes positively to strength-ductility synergy [29,30]. At or close to the eutectic composition, internal shrinkage and compositional segregation are suppressed, thereby the EHEAs are naturally suitable for large-scale industrial production [26]. Moreover, sluggish diffusion in EHEAs plays a crucial role in maintaining the thermal stability of lamellar structures, offering exceptional resistance to softening at high temperature. For instance, the as-cast $AlCoCrFeNi_{2.1}$ EHEA featuring the lamellar arrangement of FCC and BCC phases, displays a tensile strength of 1100 MPa and ductility of 18 % [27]. Notably, its remarkable mechanical properties remain nearly unchanged at the temperatures up to 700°C [26].

Leveraging lamellar or layered structures for improved tribological properties has been proven successful, because the alternating microscopic layers of varied phases can disperse local stress concentration and minimize the formation of wear debris [31–35]. Therefore, it is imperative to have a thorough comprehension of the friction and wear characteristics of EHEAs across a board temperature range to explore the materials' potential for structural applications. The enriched knowledge will aid identifying novel wear-resistant materials for practical engineering applications. The tribological characteristics of the $AlCoCrFeNi_{2.1}$ EHEA against many different counterparts, including Al_2O_3, Si_3N_4, SiC ceramics and GCr15 steel, have already been done [36]. At room temperature, the $AlCoCrFeNi_{2.1}$ EHEA displays the lowest COF and wear rate when being slidden against the SiC ceramic. For another example, the high temperature tribological performance of the $AlCoCrFeNi_{2.1}$ EHEA against Si_3N_4 ceramic is examined. A monotonous increase in wear rate with rising temperature is observed; the COF initially rose with increasing temperature from 200 to 600 °C and then sharply decreased as the temperature increased further [36]. This phenomenon is ascribed to enhanced oxidative wear and the formation of ultrafine-grained layer beneath the worn surface [36]. Tri Dinh Vo et al. investigated the effects of sizes and growth rates of oxides on the friction and wear properties of the $AlCoCrFeNi_{2.1}$ EHEA [37]. As the temperature increases from 500 to 900 °C, the wear mechanism changes from abrasion to adhesive wear; this is closely related to the development and growth of oxides [37]. Despite of encouraging advances in researching wear resistance of EHEAs, our knowledge about the high temperature wear mechanisms of EHEAs is still limited. In this work, the influence of temperature on the tribological properties of the $AlCoCrFeNi_{2.1}$ EHEA are investigated in detail. The microstructural evolutions underneath the surface of contact and the wear mechanisms governing the tribological behavior of the $AlCoCrFeNi_{2.1}$ EHEA are revealed and analyzed to explain the excellent tribological properties in a wide temperature range.

2. Experiments

The $AlCoCrFeNi_{2.1}$ EHEA ingot was casted by melting a mixture of the commercially pure constituent elements (Fe and Cr: >99.5 wt %; Al, Co and Ni: 99.9 wt %) in a vacuum induction melting furnace. The ingot was flipped and re-melted three times to ensure microstructural homogeneity. Specimens with dimensions of 20 × 5 × 2 mm^3 were cut from the ingot and subsequently ground and polished prior to the friction-

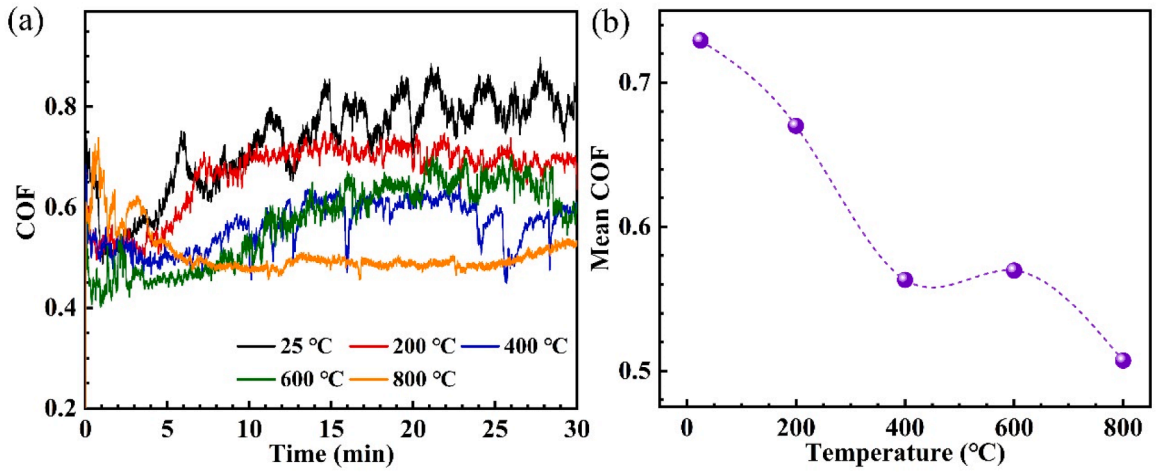

Fig 2. (a) COF vs. time curves for the $AlCoCrFeNi_{2.1}$ EHEA underwent dry sliding tests at different temperatures. (b) Variations of the mean COF with temperature.

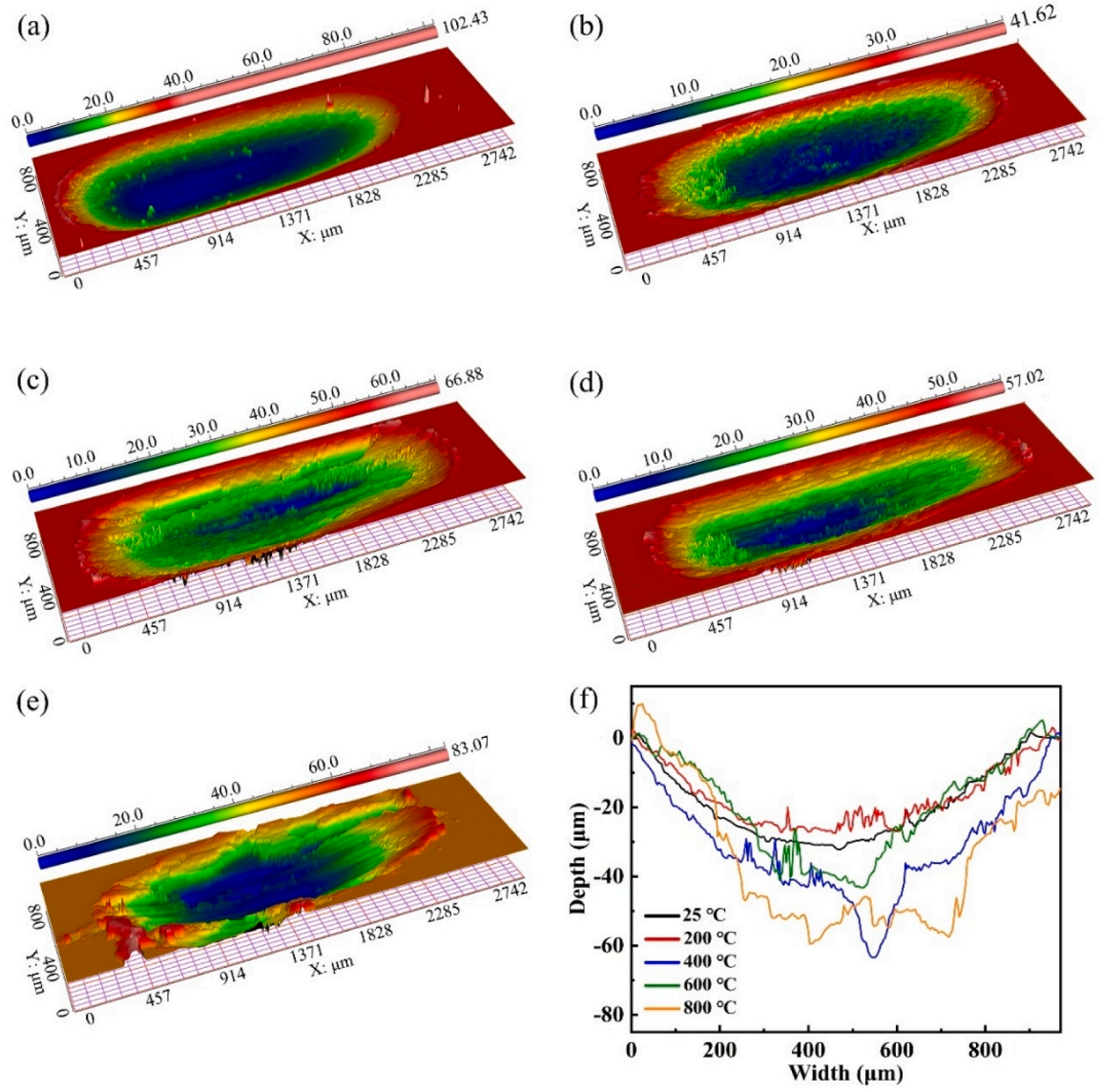

Fig 3. 3D surface morphology for the wear tracks at different temperatures: (a) 25 °C, (b) 200 °C, (c) 400 °C, (d) 600 °C, (e) 800 °C. (f) 2D profiles across transverse cross sections of the wear tracks.

wear experiment. The Si_3N_4 sphere with a diameter of 5 mm (provided by Shandong Qihang Hardware Co., LTD Co., Ltd., China) is used as the counterpart sliding against the EHEA specimens [38,39]. Reciprocating sliding friction tests were conducted with a constant normal load of 10 N and a frequency of 8 Hz for 30 min. The sliding stroke length was 2 mm and the experimental temperatures are set to 25°C, 200°C, 400°C, 600°C and 800°C. The temperature of the specimen was increased at the heating rate of 10°C/min until the target temperature, which was then maintained for approximately 3 min prior to the friction test. The COFs at different temperatures are calculated by $\mu = F/P$, where P and F are the normal applied load and frictional force, respectively.

The worn surface morphology was analyzed by the surface profilometer system (Super View W1). The wear rates are determined by the equation [40]:

$$W = \frac{V}{P \cdot L} \tag{1}$$

where V is the worn volume, P is the normal load, L is the total sliding distance. The phase structure analysis of the cast $AlCoCrFeNi_{2.1}$ EHEA was performed on the Bruker-D8 Advance X-ray diffractometer (XRD) with Cu-Kα radiation operating at 40 kV and 40 mA. The scanning angles (2θ) and scanning speed are 20°~80° and 2°/min, respectively. The compositions and microstructures of the specimens were analyzed by the Carl Zeiss-Auriga scanning electron microscope (SEM) equipped with an electron back-scattered diffraction (EBSD) system (Oxford Instruments Aztec 2.0). The EBSD specimens were prepared via a standard electropolishing process. The electrolyte comprises 10 vol % perchloric acid and 90 vol % acetic acid. The analysis of the morphology and chemical composition of the worn surface were conducted on a SEM (Quanta 250 F, FEI, Hillsboro, OR, USA) equipped with the OXFORD XMax energy dispersive X-ray spectrometer (EDS) detector. The chemical bonding states of the elements on the worn surfaces of the $AlCoCrFeNi_{2.1}$ EHEA were analyzed by means of X-ray photoelectron spectroscopy (XPS) on Thermo Fisher Scientific Nexsa with monochromatised X-ray of Al-Kα source. Microstructures of the worn surface were investigated in detail by a FEI Talos F200X G2 transmission electron microscope (TEM) equipped with SuperX energy dispersive X-ray Spectroscopy (EDS) detector. The TEM specimens were prepared by focused ion beam (FIB) milling in FEI Scios 2 HiVac dual beam SEM.

3. Results

3.1. Initial microstructures

As presented by the orientation imaging microscopy (OIM) image and phase image in Fig 1a and **b**, respectively, the as-cast $AlCoCrFeNi_{2.1}$ EHEA has the FCC/BCC eutectic lamellae structure. The volume fraction of the BCC phase is approximately 33 %, and the rest is the FCC phase. The dual-phase microstructure is also corroborated by the XRD pattern in Fig 1c. According to the SEM-EDS analysis result shown in Fig 1d, the FCC $L1_2$ phase is rich in Co Cr, Fe and Ni, and the BCC B2 phase is rich in Al and Ni.

3.2. COFs and specific wear rates

Figure 2a exhibits the variations of COF with respect to sliding time for the $AlCoCrFeNi_{2.1}$ EHEA at different temperatures. As shown in Fig 2a, all curves show large fluctuations at the running-in stage, this is attributed to the strain hardening and initial fracture of the worn surface [14,36]. At 25°C, the COF-time curve shows large fluctuations which are attributed to the complex physical and chemical interactions involving three-body abrasion, periodic localized fractures of the surface layer, and the periodic deposition and removal of debris [14,41]. Similar phenomena have also been reported for $CoFeNi_2$ MEA [42], AlCoCrFeNi HEA [14] and AlCoCrCuFeNi HEA [43]. COF is sensitive to temperature,

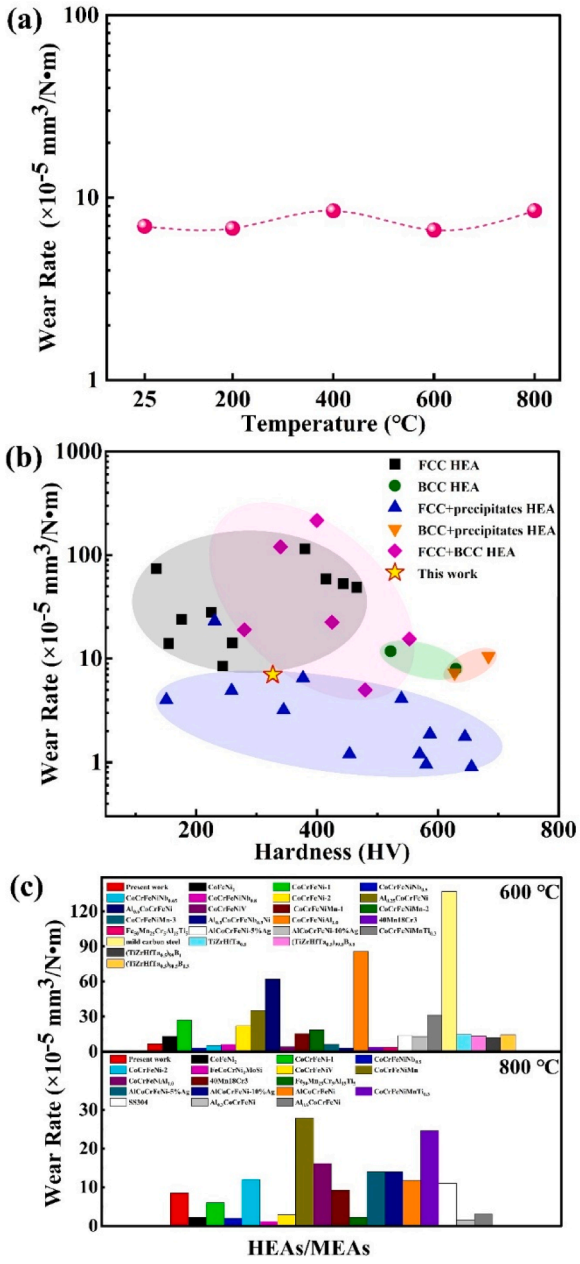

Fig 4. (a) Variations of wear rate with respect to temperature. (b) The relationship between wear rate and hardness at 25 °C for the $AlCoCrFeNi_{2.1}$ EHEA and other referenced HEAs [14,16,41,44–58]. (c) Wear rates for the present $AlCoCrFeNi_{2.1}$ EHEA and other referenced HEAs at 600 °C and 800 °C [14,17,41,42,46,57,60–68].

the magnitudes of fluctuations were small at 200°C, 600°C and 800°C, but at the 400°C there were multiple large drops of COF. As shown in Fig 2b, the mean COF decreases from ~0.73 at 25 °C to ~0.51 at 800 °C as a general trend, but an interim plateau is seen between 400 °C and 600 °C. At elevated temperatures, the fairly smooth friction trace is usually related to oxide coverage on the worn surface, which will lead to the reduction of COF [14].

Figure 3a-e display the 3D surface morphology of the worn tracks on the $AlCoCrFeNi_{2.1}$ EHEA. Fig 3f shows the 2D profiles across the deepest transverse sections of the worn tracks. At 25 °C, the worn track is relatively shallow (Fig 3f), with a smooth bottom and edges (Fig 3a). As the temperature increases, the depths of the worn track increases, and the worn surfaces exhibit increasing roughness (Fig 3a-e). At 800 °C, large accumulation of materials is realized along the edge of the worn track

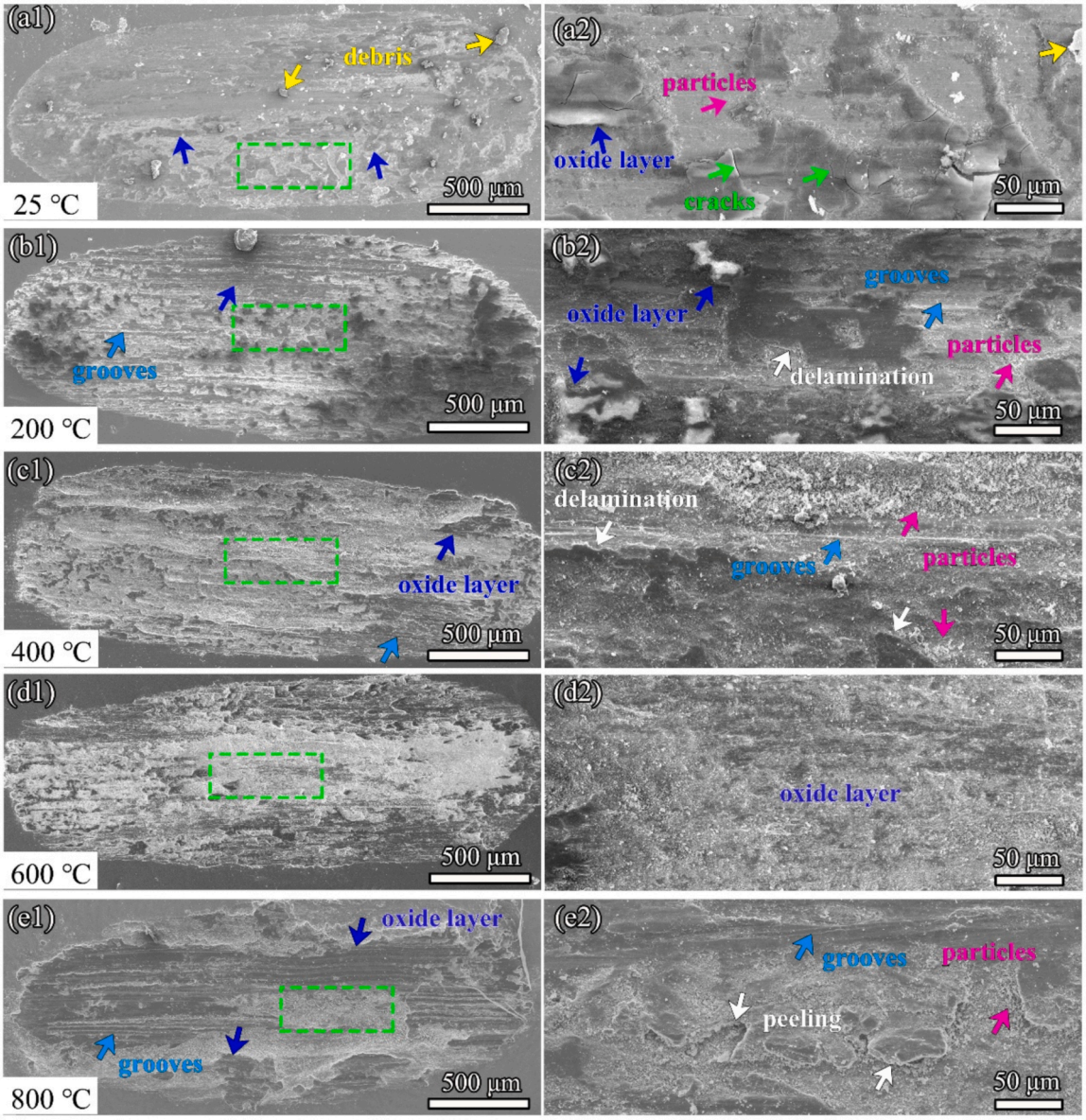

Fig 5. Worn surfaces of the $AlCoCrFeNi_{2.1}$ EHEA at different temperatures: (a1-a2) 25 °C, (b1-b2) 200 °C, (c1-c2) 400 °C, (d1-d2) 600 °C, (e1-e2) 800 °C.

(Fig 3e).

The variation of wear rate with respect to temperature is depicted in Fig 4a. Fig 4b compares the wear rate and hardness at 25 °C for the $AlCoCrFeNi_{2.1}$ EHEA and several referenced HEAs, including single phase HEAs and dual-phase (FCC+BCC) systems [14,16,41,44–58]. Generally, wear of most HEAs adheres to Archard's relationship [59], that is, the wear rate is proportional to the materials hardness. However, the present $AlCoCrFeNi_{2.1}$ EHEA demonstrates a low wear rate despite its relatively low hardness, suggesting that the presence of eutectic lamellae significantly bolsters its inherent wear resistance. Notably, the wear rate of the $AlCoCrFeNi_{2.1}$ EHEA remains stable up to 800°C, indicating excellent thermal resistance and anti-wear performance across a broad temperature range. According to literatures, the wear rate does not vary linearly with changing temperature. For instance, the wear rates of $CoCrFeNiNb_x$ and AlCoCrFeNi alloys initially increase and then decrease within the temperature range of 25-800°C, peaking at 400 °C [38,46]. The $CoFeNi_2$ MEA exhibits peaked wear rates at 600°C [42]. On the other hand, the wear rate of an $Al_{0.25}CoCrFeNi$ HEA markedly increased in the temperatures 20-300 °C and remained nearly constant at temperatures 300-600°C [41]. Moreover, the CoCrNi MEA showed continuous reduction in wear rate with increasing temperature up to 300 °C [53]. In comparison to many HEAs and MEAs, the wear rates of present $AlCoCrFeNi_{2.1}$ EHEA at 600°C and 800°C is among the lowest order of magnitude, as shown in Fig 4c [14,17,41,42,46,57,60–68]. The wear rates of HEAs/MEAs at elevated temperatures are influenced by multiple factors, including the chemical compositions, the oxidation layer, and the stress/strain distribution beneath the contact surface.

3.3. *Worn surface morphology*

Figure 5 exhibits the worn morphologies of the $AlCoCrFeNi_{2.1}$ EHEA at different temperatures. As shown in Fig 5a1, there are patches and debris on the worn surface. The boxed area in Fig 5a1 is enlarged in Fig 5a2, thins cracks can then be seen on the patches, suggesting that the patches are brittle. As the temperature increased to 200 and 400 °C, delamination fracture occurred to expose the fresh metal underneath as shown in Fig 5b1 and **c1**, respectively. Fig 5b2 and **c2** are high magnification images showing grooves and fine particles on the worn surfaces. At 600 °C, delamination fracture was suppressed; Patches were no longer identifiable; The oxide layer was dense and has a good integrity,

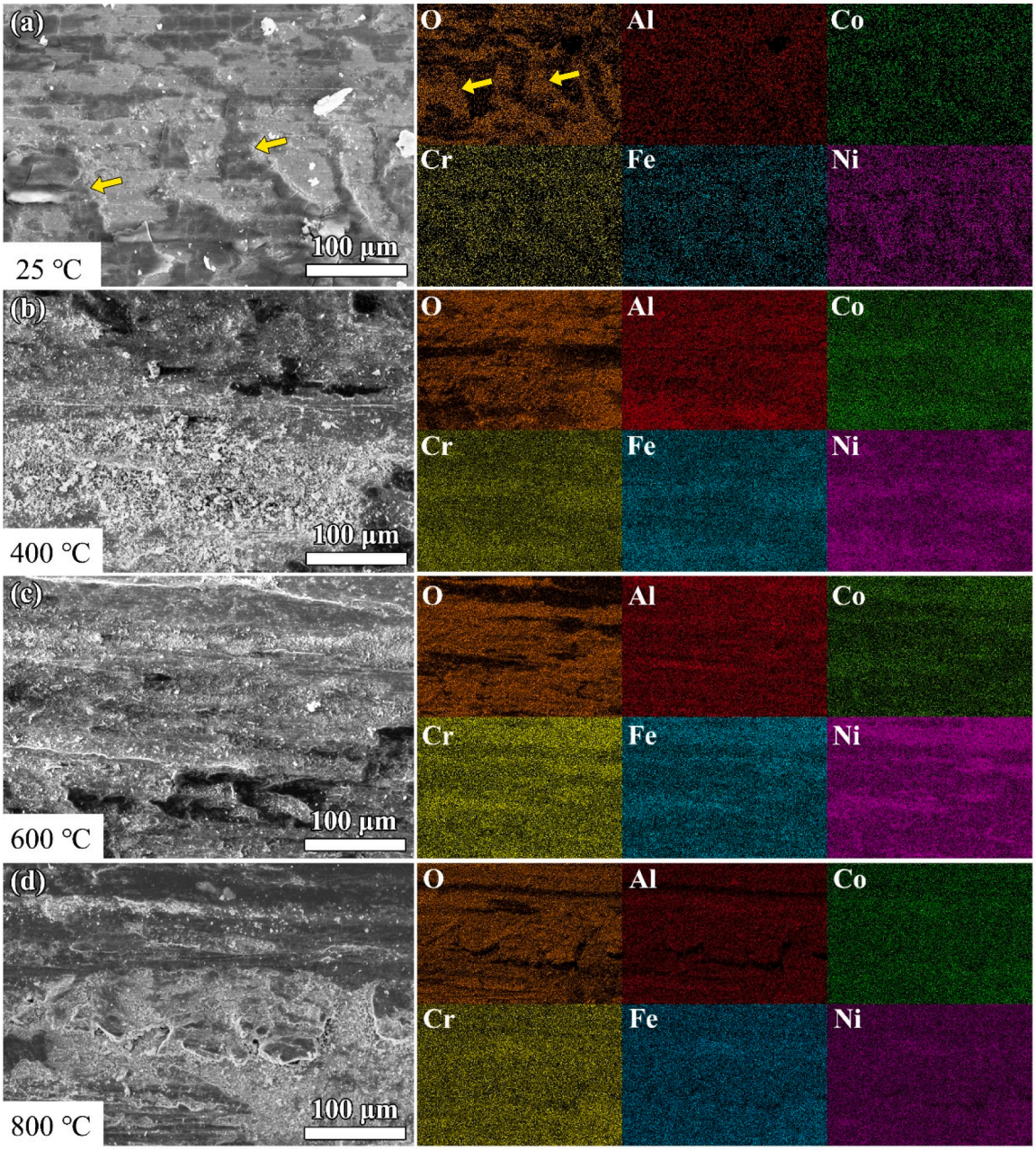

Fig 6. SEM images and corresponding EDS mapping of Al, Co, Cr, Fe, Ni and O elements on the worn surfaces of the $AlCoCrFeNi_{2.1}$ EHEA at different temperatures: (a) 25 °C, (b) 400 °C, (c) 600 °C, (d) 800 °C.

Table 1
Chemical compositions (at %) on the worn surfaces at different temperatures.

Temperature	Al	Co	Cr	Fe	Ni	O
25 °C	9.3	9.4	9.5	9.4	19.4	43
400 °C	8.9	9.2	9.4	9.3	19	44.2
600 °C	8.6	8.8	8.9	8.7	18	47
800 °C	7.6	7.7	8.1	7.8	15.3	53.5

as shown in Fig 5d1 and d2. As the temperature further ascended to 800 °C, oxide layers were partly peeled off or scratched off, leaving long grooves on the surface, as shown in Fig 5e1. Enlarged image in Fig 5e2 show large peeling pits and numerous oxide patches on the worn surface.

Figure 6 presents the EDS mapping of Al, Co, Cr, Fe, Ni and O elements on the worn surfaces at different temperatures. The quantified chemical composition (at %) are presented in Table 1. As shown in Fig 6a, the patches observed at 25 °C are rich in O element, indicating that friction induces the formation of oxides. The content of O at 25 °C is about 43 at %. With temperature increased, the O element distribution on the friction surface becomes more uniform and the content of O increases gradually, up to 53.5 at % at 800 °C. Notably, there are local oxygen-deficient regions at 400, 600 and 800 °C. These regions might be exposed fresh metal underneath, showing enrichments of Co, Cr, Fe and Ni elements.

XPS analysis were performed on the oxidized tribo-layers. As illustrated in Fig 7, the tribo-layer of $AlCoCrFeNi_{2.1}$ EHEA at 25 °C contains various types of oxides. Notably, the intermetallic $AlNi_x$ phase is abounding in the Al_{2p} spectrum across all temperatures tested. The intermetallic $AlNi_x$ phase has been reported to impart resistance against

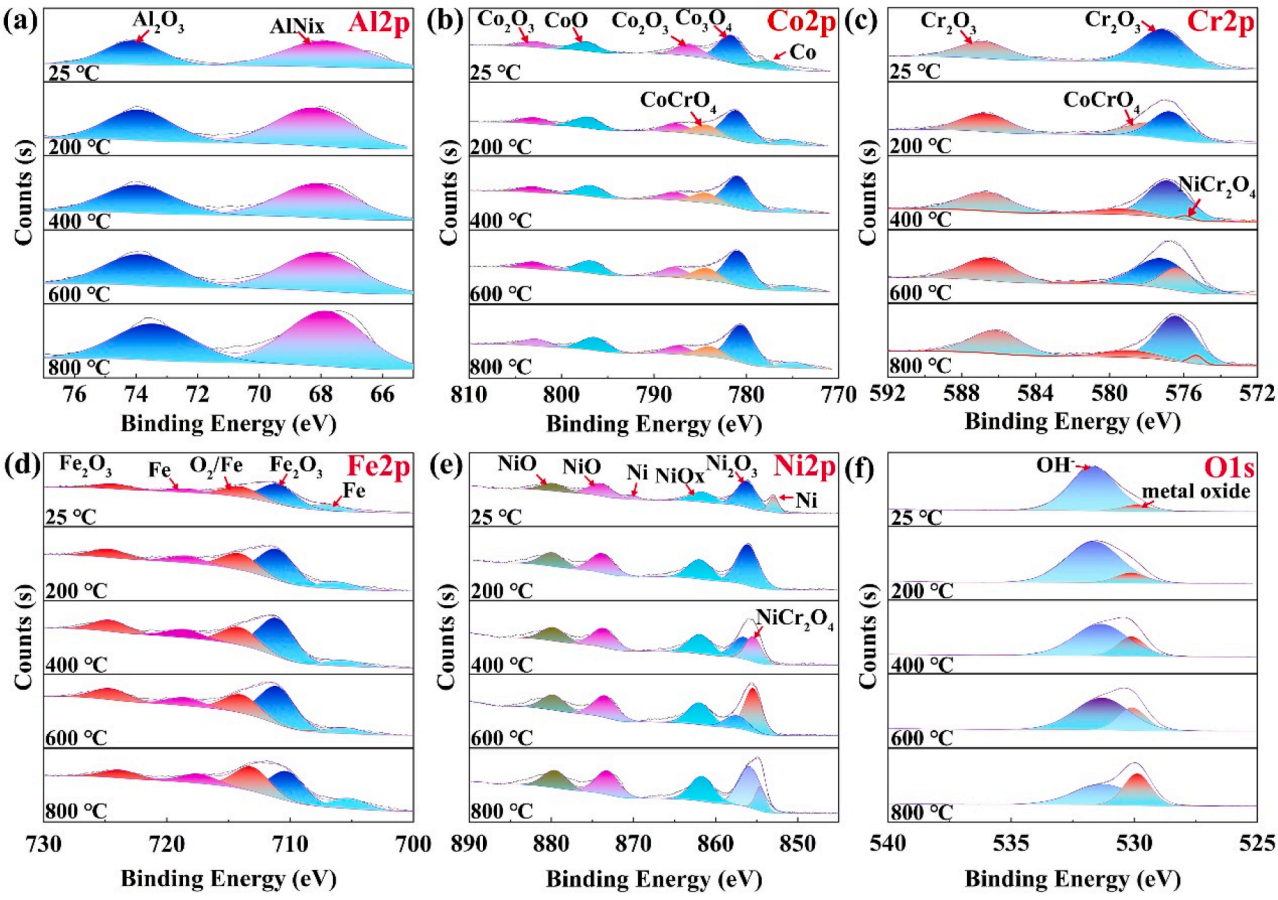

Fig 7. (a) Al_{2p}, (b) Co_{2p}, (c) Cr_{2p}, (d) Fe_{2p}, (e) Ni_{2p} and (f) O_{1s} spectra on the worn surfaces of the $AlCoCrFeNi_{2.1}$ EHEA at different temperatures by XPS analysis.

plastic deformation and to prevent the formation of abrasive particles [38]. At 25 °C, metallic Co, Fe and Ni are detected, indicating partial oxidization of the alloy. As the temperature increased, the metallic Ni spectrum vanished, while Co and Fe spectrums also progressively attenuated, reflecting enhanced oxidation effects. Concurrently, the relative intensity of metal oxide peaks increased with temperature, corroborating a vigorous oxidation process during sliding [69]. Intriguingly, residual metallic Co and Fe spectra persisted even at 800°C, presumably due to substrate exposure caused by peeling off of oxide layer.

Weak $CoCrO_4$ signals at 200 °C are seen in Fig 7b and c; $NiCr_2O_4$ signal at 400 °C are seen in Fig 7e. In this Ni- and Al-rich EHEA system, thermal activation promotes Cr incorporation into complex oxide structures, such as $CoCrO_4$ and $NiCr_2O_4$ [46]. The $NiCr_2O_4$ signal intensity gradually increases to the maximum at 600 °C, whereas $CoCrO_4$ signals remains relatively stable across the temperature range. Monotonic decrease in hydroxyl (OH^-) contribution with increasing temperature is seen in the O_{1s} spectrum in Fig 7f. This trend is attributed to reduced atmospheric moisture adsorption at elevated temperatures. Additionally, surface contaminants such as physisorbed water and hydroxyl groups may have contributed to the OH^- signal intensity.

The subsurface structures were examined for the objective of gaining insight into the underlying wear mechanisms at varied temperatures. Fig 8 presents the microstructures beneath the worn surface at 25 °C. In accordance with the observed diffraction contrast in grain morphology within the bright field (BF) TEM image and corresponding HAADF-STEM image, the cross-sectional region may be divided into three distinct regions: the topmost oxidation layer, the refined nano-lamellar layer and the coarse-grained region (the red and yellow dash lines delineate three regions in Fig 8a and b). In the vicinity of sliding contact surface, an oxidation layer with a thickness range of 60-250 nm serves as a protective layer, as indicated by the EDS mapping results presented in Fig 8g. Fig 8c-1 depicts the detailed examination of the microstructures in the oxidation layer with light contrast, where dark spots are randomly distributed. Wang et al. suggested that the amorphous area is brighter than the crystalline one, because an amorphous structure does not produce strong electron diffraction [70]. The HRTEM image (Fig 8c-2) and the corresponding selected area electron diffraction (SAED) pattern reveal randomly oriented nanograins that are embedded within the amorphous substrate. Within the topmost oxidation layer, cracks are observed, as shown in Fig 8a.

Beneath the topmost oxidation layer, we showcase the refined nano-lamellar layer (Fig 8a). As illustrated in Fig 8d, friction shear strain induces severe plastic deformation to the original coarse grains, leading to the formation of lamellar nanograins extending to a depth of 2 μm. The average thickness of the nano-lamellar is approximately 21 nm. At the bottom-right corner of Fig 8a, the thicknesses of the lamellar grains are larger, attributed to reduced plastic strain away from the surface. Notably, some bright contrast zones (marked by white arrows) are embedded in the nano-lamellar layer in the form of inter-lamellae, as shown in Fig 8e and **f-1**. As evidenced by the EDS element mapping in Fig 8g, the aforementioned areas are characterized by an enrichment of O element. The HRTEM image and corresponding SAED pattern in Fig 8f-2 unveil the nanocrystalline-amorphous composites within the bright contrast zones. In the HAADF-STEM image, the regions of the nanocrystalline-amorphous composites have a dark contrast (same in the later analysis), as shown in Fig 8b. With the friction proceeds, the nanocrystalline-amorphous composites will expand along the sliding direction, as shown in Fig 8e. Beneath the nano-lamellar layer, the coarse grains deform mainly by dislocation slip, leading to high dense

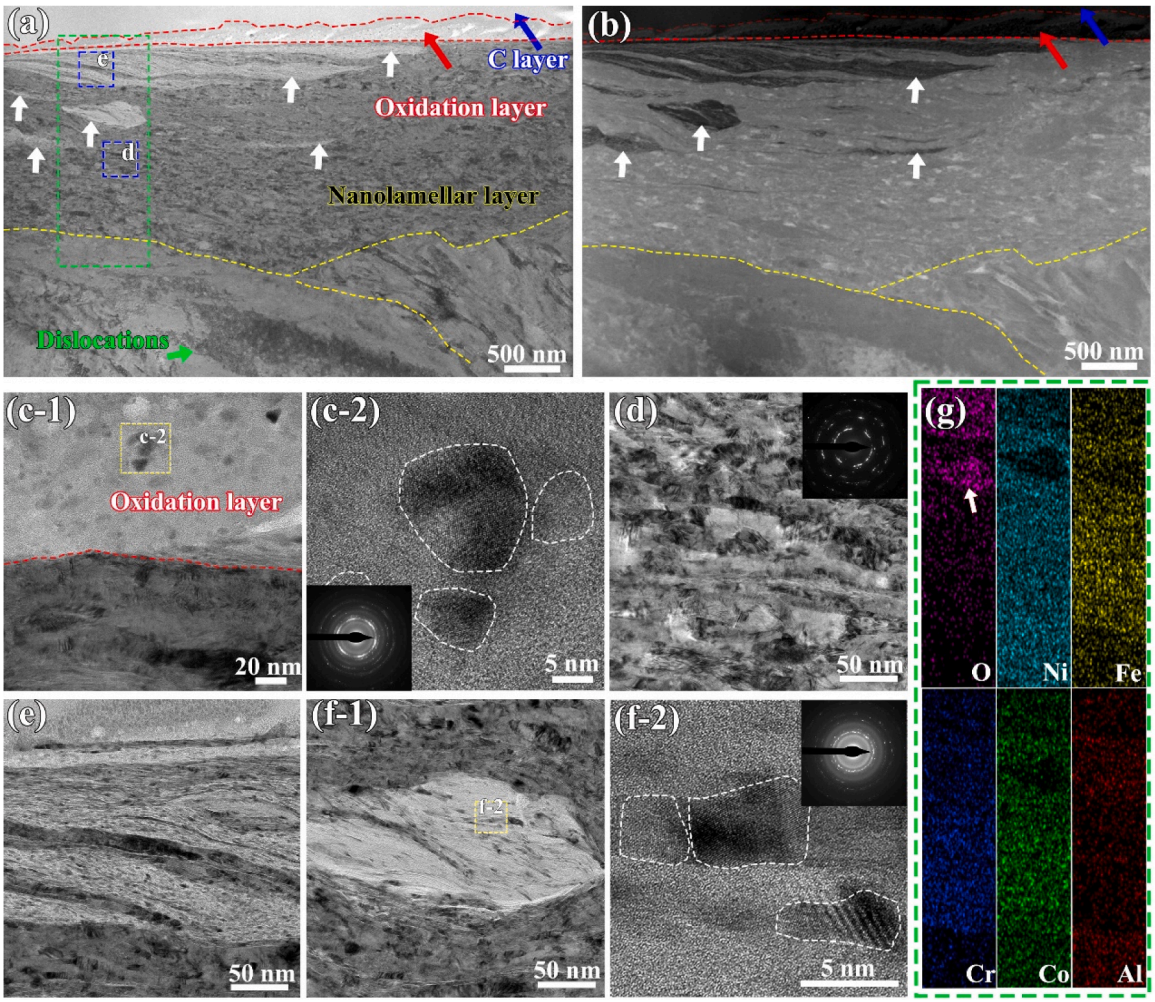

Fig 8. FIB cross-sectional TEM characterization of the $AlCoCrFeNi_{2.1}$ EHEA after dry sliding at 25 °C. (a, b) Bright field TEM image and the corresponding HAADF-STEM image of the subsurface microstructures. (c-1) STEM image of the topmost oxidation layer. (c-2) HRTEM image of boxed area in c-1. (d) STEM image of the nano-lamellar layer. (e) STEM image of the blue-boxed area in (a), showing the lamellar structure. (f-1) STEM image showing a typical bright contrast zone in the nano-lamellar layer. (f-2) HRTEM image of the yellow-boxed area in (f-1). (g) EDS mapping of the green-boxed area in (a).

dislocation substructures. No cracks nor micro-voids are discernible in the nano-lamellar layer and the coarse grains matrix.

Fig 9 depicts the subsurface microstructures of the $AlCoCrFeNi_{2.1}$ EHEA tested at 400 °C. As shown in the BF TEM image and corresponding HAADF-STEM image, the worn subsurface features the nanostructured layer region sandwiched between the oxide layers (Fig 9a and **b**). The set of EDS maps confirm O element in the oxide layers (Fig 10). HRTEM analysis further resolves these oxide layers as nanocrystalline-amorphous composites, as shown in Fig 9c and **e**. Within the nanostructured layer, the original coarse grains are refined into equiaxed nano-grains with an average grain size of 13 nm (Fig 9d-2). In the nanostructured layer, regions displaying similar contrast to the oxide layer (marked by green arrows in Fig 9a and **b**) are found to contain similar nanocrystalline-amorphous composites (Fig 9d-1 and **d-3**). Notably, **d-1** region has a higher amorphous content than **d-3** region, as confirmed by HRTEM analysis. Therefore, it is plausible to infer that region **d-3** represents the transition state between nanostructure to amorphous phases. Crack propagation is detected in both oxide layers and the nanostructured layer, and the cracks are marked by white arrows in Fig 9a and **b**. HRTEM characterization at crack tips (Fig 9f) reveals fully amorphous structures, indicating that local plastic deformation during sliding promoted amorphization [71], which in turn facilitated crack nucleation.

At 800 °C, the subsurface region beneath the worn surface is dominated by continuous oxide layer, as shown in Fig 11a and **b**. Many cracks are seen in the oxide layer, indicating poor interfacial adhesion at 800 °C. At the topmost surface, an amorphous layer with a thickness of ~50 nm is identified in Fig 11c-2 and the typical diffused diffraction ring for amorphous structure is seen in the fast Fourier transforms (FFT) pattern. Beneath the topmost amorphous layer, all the oxide layers in the observation field present a crystalline structure, as shown in Fig 11d-1, d-2 and **f**. This is different from the nanocrystalline-amorphous composites observed at 25 °C and 400 °C, suggesting that there is a thermally activated dynamic crystallization process at 800 °C.

Within the inner crystalline oxide layer, some equiaxed recrystallized grains with an average grain size of 246 nm are detected, as shown in Fig 11e. The recrystallization is attributed to the high-temperature exposure [72,73], consistent with prior reports on 90 % cold-rolled $AlCoCrFeNi_{2.1}$ EHEA, where annealing at 800 °C produces recrystallized ultrafine grains with exceptional thermal stability up to 1200 °C [74]. There are ordered $L1_2$ phases within the recrystallized grains, as evidenced by the superlattice spots marked by yellow circles in Fig 11e. EDS maps in Fig 12 confirm homogeneous oxygen distribution throughout the oxide layer, and some recrystallized grains with weak signals for oxygen.

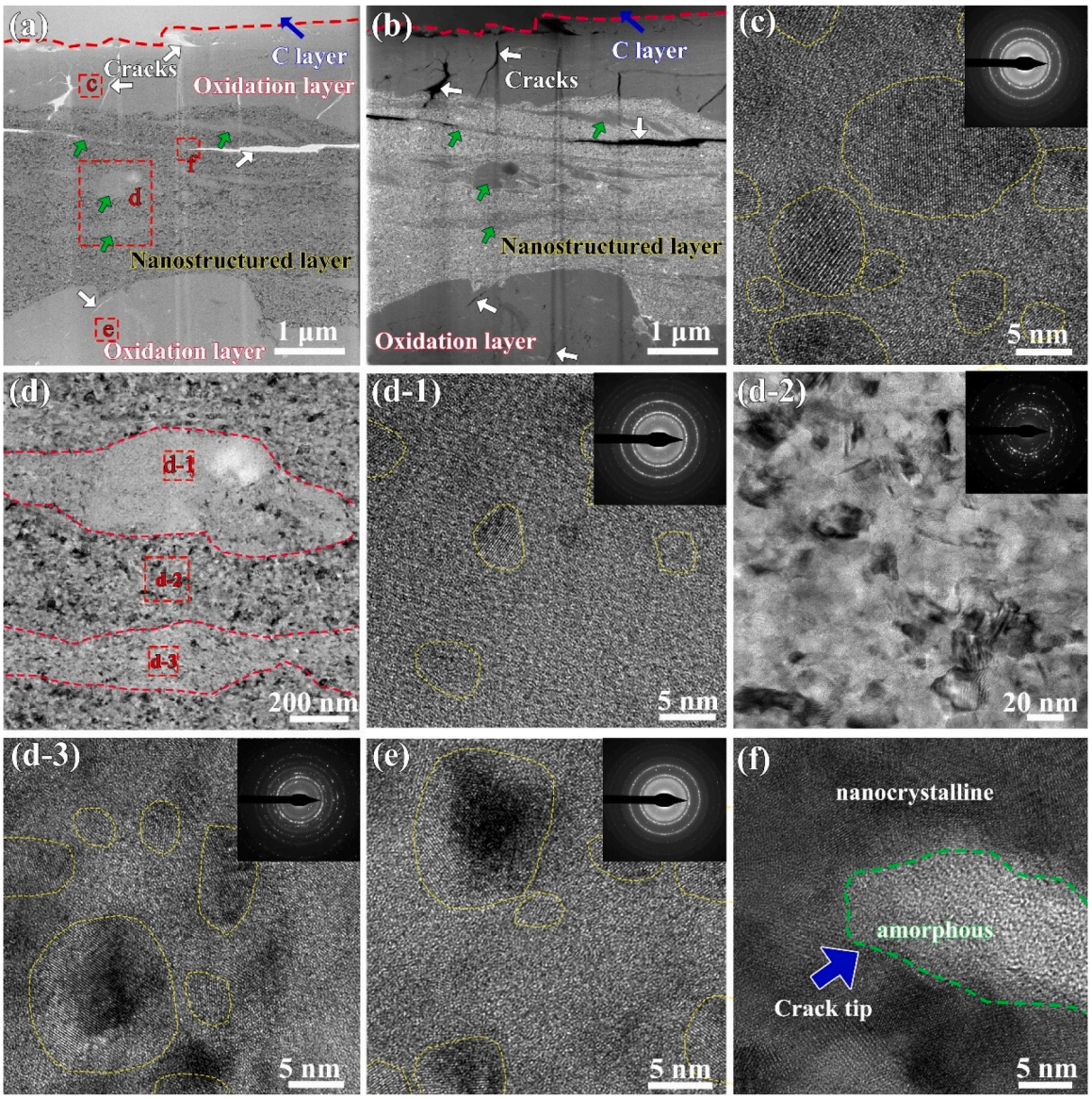

Fig 9. FIB cross-sectional TEM characterization of the $AlCoCrFeNi_{2.1}$ EHEA tested at 400 °C. (a, b) Bright field TEM image and the corresponding HAADF-STEM image of the subsurface microstructures. (c) HRTEM image of the red-boxed area in (a), showing the nanocrystalline-amorphous composites in the topmost oxidation layer. (d) A high magnification TEM image of the red-boxed area in (a). (d-1) and (d-3) HRTEM image of the selected area in (d), demonstrating the nanocrystalline-amorphous composites. (d-2) A zoom-in TEM image of the selected area in (d), demonstrating the nanograin structures. (e) HRTEM image of the red-boxed area in (a), demonstrating the nanocrystalline-amorphous composites in the bottom oxidation layer. (f) HRTEM image of the selected area in (a), demonstrating the amorphous structure at the front tip of the crack.

4. Discussions

4.1. Formation mechanisms for the nanocrystalline-amorphous composites

The nanocrystalline-amorphous composite structures are discernible in the subsurface of the $AlCoCrFeNi_{2.1}$ EHEA after dry sliding at 25 and 400 °C, as shown in Fig 8 and Fig 9. The amorphization process involves mechanical alloying, which is commonly observed from dry sliding wear [75]. The amorphous oxides develop from squeezing, grinding, and mixing of wear debris and particles at the surface of contact [76]. Frictional heating elevates the average temperature on the contact surface to several hundred degrees, while the localized contact zones can reach even much higher temperatures [77]. The concurrent action of thermal heating (friction heat and/or ambient heat) and oxygen diffusion facilitates the oxidation and solid-state amorphization (SSA) transition process at the topmost layer [70,78–80]. It is the severe plastic deformation at the surface caused the crystalline-to-amorphous transition [70,81,82]. A high density of dislocations associated with accumulated plastic strain increases the microscopic shear stress to a critical value for amorphization [70] (according to literatures, the maximum equivalent strain and shear strain induced by friction can reach 21 and 77, respectively [83,84]). In present $AlCoCrFeNi_{2.1}$ EHEA, the high density of dislocations that triggers SSA is attributed to the microstructural characteristics. Firstly, high concentrations of solute atoms and enhanced lattice distortions induced by elastic modulus mismatch and atomic-size mismatch [85] offer the intrinsically high lattice resistance to dislocation slip [86]. The average atomic size differences δ in FCC and BCC phases in $AlCoCrFeNi_{2.1}$ EHEA are 0.038 and 0.071, respectively, larger than that of 0.0207 in CrMnFeCoNi HEA [86]. Secondly, the presence of nano-precipitates in the BCC phase promotes multiplication of dislocations via the pinning effect [27]. Thirdly, the

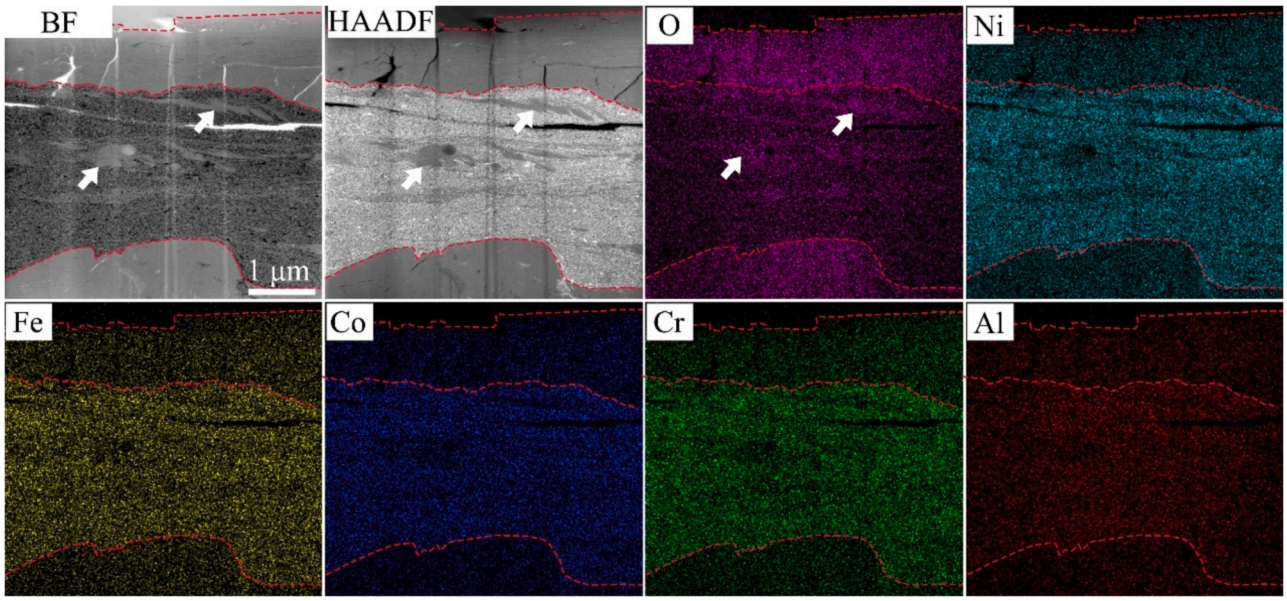

Fig 10. Bright field TEM and HAADF image, and the corresponding EDS elemental maps for the $AlCoCrFeNi_{2.1}$ EHEA after dry sliding at 400 °C.

semi-coherent interfaces between FCC and BCC phases act as effective barriers to dislocation slip [30]. Finally, continuous built-up of shear strain under friction sliding introduces extra dislocation boundaries and sub-grain boundaries via the grain refinement, resulting in significantly increased shear stress [87]. To sum up, the intrinsically high lattice resistance, the pinning effect of nano-precipitates, the presence of interphase interfaces and the increasing number of dislocation boundaries jointly raised the local dislocation density to a critically high level and so does the shear stress. Then, the excess free energy of the system eventually leads to crystal instability, collapse of the ordered lattice structure, in other words, amorphization [76]. Usually, the stress concentration leads to high free energy at the crack tip, thus amorphization occurs at the crack tip as shown in Fig 9f [70].

Oxygen atoms play a crucial role in crystalline-to-amorphous transition. As evidenced by the EDS maps in Fig 8g and Fig 10, the regions of nanocrystalline-amorphous composite are rich in O elements. During the friction sliding process at 25 °C, the abundant grain boundaries featuring high-density dislocations and lattice distortions, serve as fast pathways for the oxygen atoms diffusion [88]. According to the empirical law of glass-forming, incorporating oxygen atoms into the alloy modifies the atomic coordination and directional bonding, and may result in a large negative enthalpy of mixing. These chemical reactions promote amorphization [89–91].

At the high temperature of 400 °C, the thickness of the oxidation layer containing nanocrystalline-amorphous composites significantly increases, even for those beneath the nanostructured layer (Fig 9). Numerous cracks are visible in the oxidation layer and nanostructured layer, acting as N channels for the transfer of oxygen atoms. The oxygen atoms can quickly go through the cracks to reach and oxidize the disordered atomic structures and thus to accelerate amorphization of the nanostructure. Particularly at crack tips with high stress concentrations, the increased free energy induced by dislocations activities and point defects attracts oxygen [76], accelerating the amorphization process of the nanostructure (Fig 9f). In conjunction, the absorption of oxygen atoms further reduces the lattice rigidity and facilitates the expansion of amorphous areas (Fig 9a and b) [92].

However, there exists a dynamic competition between the crystalline-to-amorphous transition and the reverse crystallization process of amorphous structures due to the combined effect of ambient and friction heat. At 800 °C, the amorphous structures are detected solely at the topmost surface, attributed to constantly mechanical alloying (squeezing, grinding, and mixing of wear particles) [75,76]. It is plausible for amorphous oxide to undergo crystallization again, given the enhanced kinetic energy of atomic diffusion at high temperatures [93]. The dynamic recrystallisation behaviors under sliding wear have been observed in CoCrFeMnNi and $Al_xCoCrFeNi$ HEAs, and have been attributed to local plastic deformation with large strains and frictional heat accumulations beneath the worn surfaces during dry sliding friction at a very high operating temperature [14]. The stress concentration sites induced by non-uniform crystallization (Fig 11e) become the sources of cracks when subjected to external forces. Consequently, numerous cracks are detected throughout the oxide layer at 800 °C (Fig 11a and **b**).

4.2. *Friction and wear mechanisms at different temperatures*

The $AlCoCrFeNi_{2.1}$ EHEA exhibits decreasing trends for COF and stable wear rate with the temperature being increased from 25 to 800 °C. This is closely related to the friction and wear mechanisms at elevated temperatures. At 25 °C, the discontinuous oxide layers on surface (Fig 5a1) suggest oxidation-induced wear [94]. The formation of intermetallic $AlNi_x$ phase resists further plastic deformation and prevents the formation of abrasive particles, contributing to the low wear rate at 25 °C [38]. Micro-cracks form in the oxide layers, indicating the fatigue wear under repeated sliding [95,96].

With the temperature increased to 600 °C, delamination fracture (Fig 5b1 and **c1**) was dominant, and is related to the inferior mechanical properties and bonding strength of oxide layers [97]. Under the action of ambient and friction heat, inorganic acid salts, $CoCrO_4$ and $NiCr_2O_4$ form on the worn surface (Fig 7). In general, the inorganic acid salts is bridging to the formation of the compact oxidized tribo-layers (also known as glaze layers), which can help avoid direct contact and adhesion of micro-bulge between friction pair interfaces [98]. The compact oxidized tribo-layer (Fig 5d2) plays a pivotal role in safeguarding metals against direct contact, thereby conferring a markedly diminished wear rate [95,96,99,100]. Besides, the increased number of particles on the surface of the oxide layer reduces the mean COF at 25-400 °C owing to the particles rolling action [99].

At 800°C, the yield strength of the $AlCoCrFeNi_{2.1}$ EHEA is decreased due to thermal softening. The debris scattered on the worn surface had a ploughing effect during dry sliding friction, leaving many parallel grooves (Fig 5e1). Nevertheless, rolling of these particles reduces the mean COF (Fig 2b).

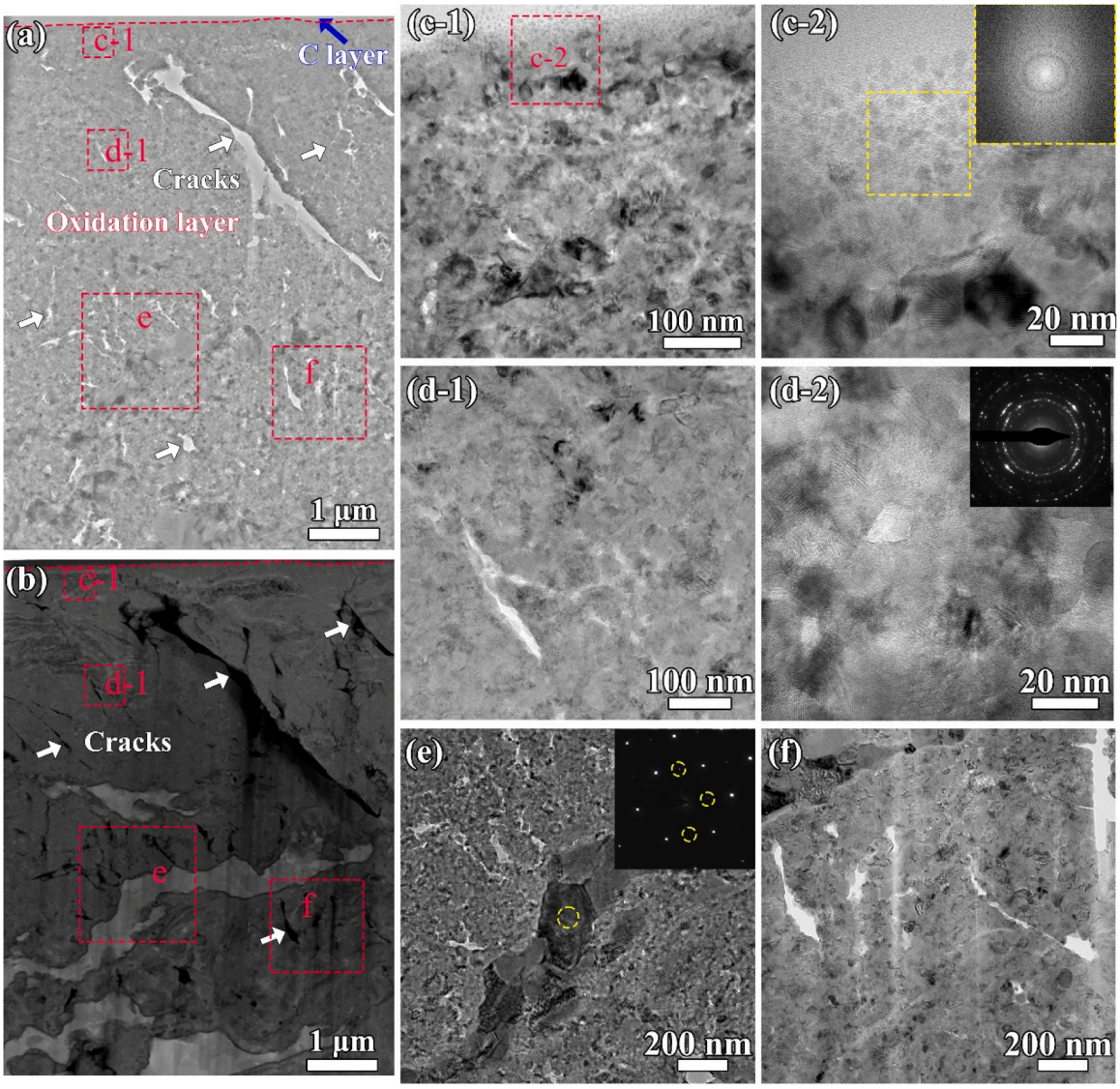

Fig 11. FIB cross-sectional TEM characterization of the $AlCoCrFeNi_{2.1}$ EHEA after dry sliding at 800 °C. (a, b) Bright field TEM image and the corresponding HAADF-STEM image of the subsurface microstructure. (c-1) STEM image of the red-boxed area in (a). (c-2) HRTEM image and the corresponding FFT pattern, demonstrating the amorphous structure at topmost layer. (d-1) STEM image of the red-boxed area in (a). (d-2) HRTEM image and corresponding SAED pattern showing the nanocrystalline structure. (e) STEM image of the red-boxed area in (a) and the corresponding SAED pattern, showing ultrafine-grained structures. (f) STEM image of the red-boxed area in (a), showing the nanocrystalline structure.

4.3. Anti-wear mechanism of composite oxide layer

Hardness and strength play crucial roles in affecting the wear resistance of materials. Both nanograins and amorphous structures possess high strength and hardness [87,101]. However, the nanograined metallic materials are usually brittle with little plastic deformation ability [87]. Amorphous alloys deform plastically via activation and motion of shear bands [102] that can propagate rapidly and resulting in catastrophic failure and thus negligible macroscopic ductility [103]. Therefore, in addition to high strength and hardness, homogeneous plastic flow ability is also importance for high wear resistance, such as gradient nanograined materials with enhanced wear resistance [19]. The homogeneous plastic deformation of amorphous alloys can be realized by reducing the amorphous regions to below 100 nm [104]. Amorphous-crystalline nanocomposites have been reported to have outstanding strength-deformability combination and remarkable wear resistance [69,89,105], so does the current case. The mutually compatible flow behavior between amorphous and crystalline phases can effectively accommodate the wear-induced plastic deformation [69,105]. Moreover, the dispersed nanocrystals can effectively impede propagation of local shear bands in the amorphous matrix via the grain rotation mechanism [4,105]. In contrast, the fully amorphous structures formed on the surface of VCoNi film fail to accommodate the wear-induced plastic deformation, leading to higher wear rate [69]. Thus, in this experiment, the nanocrystalline-amorphous composite layers formed during dry sliding friction of $AlCoCrFeNi_{2.1}$ EHEA have high strength, and can reduce the propensity of strain localization, promote uniform deformation and prevent coalescence of micro-crack.

Nano-grains were generated via dynamic recrystallization under dry sliding friction at 800 °C, but grain coarsening was insignificant. The high strength and hardness of nanostructures (nanograins and ultrafine grains) are favorable factors for wear resistance, but their brittleness prejudices the accommodation of the wear-induced plastic deformation, leading to numerous cracks. The material is spalled to form particles. However, under the action of friction heat and ambient heat, amorphous layer is formed on the topmost surface by complex metallurgical reactions including squeezing, grinding, mixing of wear particles and mechanical alloying, as evidenced by Fig 11c-2, contributing to

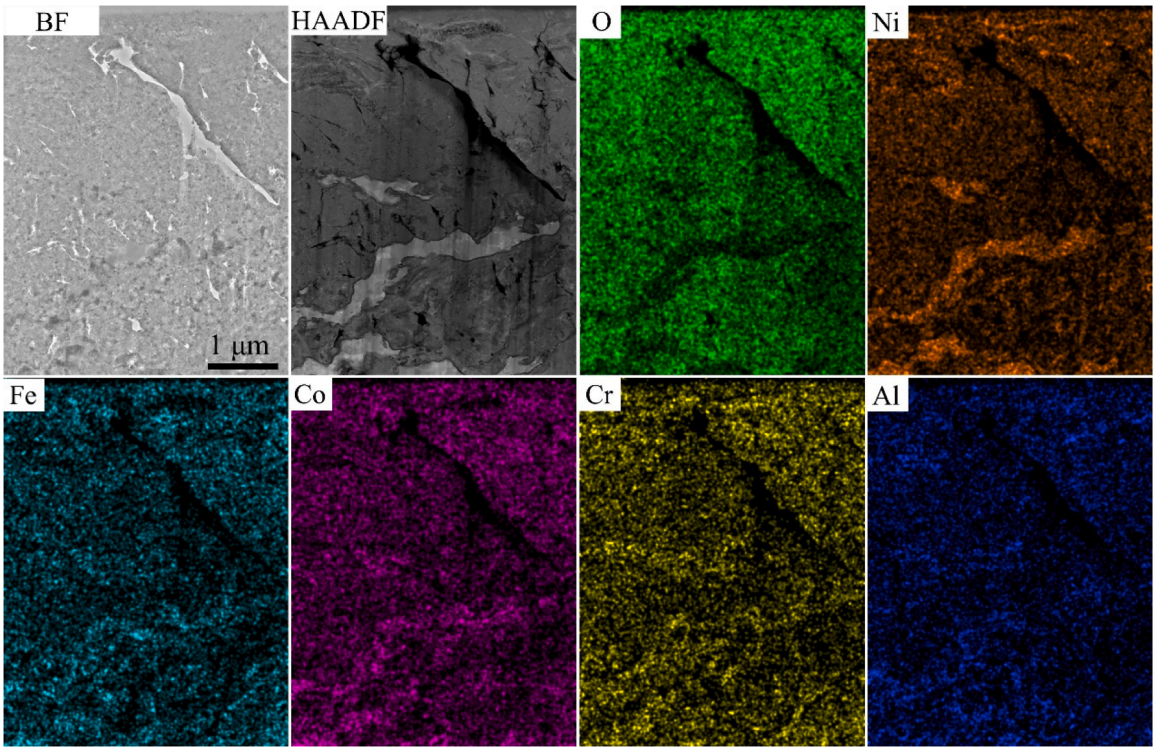

Fig 12. Bright field TEM and HAADF image, and the corresponding EDS elemental maps for the $AlCoCrFeNi_{2.1}$ EHEA after dry sliding test at 800 °C.

improved wear resistance.

5. Conclusions

In summary, high-temperature tribological behavior and wear mechanisms of the $AlCoCrFeNi_{2.1}$ EHEA are investigated over a wide temperature range 25-800 °C. The friction-induced oxidation contributes to the formation of nanocrystalline-amorphous composite layer in the subsurface. The composite layer has a high strength, and can disperse strain localization and delay coalescence of microcracks. Therefore, the composite layer is considered a protective layer against wear for the $AlCoCrFeNi_{2.1}$ EHEA at 25 °C. The EHEA exhibits the decreasing trends for COF and stable wear rates, with increasing temperature. The combined effect of friction and oxidation leads to increased thickness of the oxidation layer, providing effective protection for the EHEA underneath. At 800 °C, such high temperature enhances atomic diffusion, thus the amorphous oxide layers undergo partial crystallization to form nanocrystals. The nanostructures in $AlCoCrFeNi_{2.1}$ EHEA are thermal stability with only localized ungrown recrystallization and their high hardness is beneficial to anti-wear performance.

CRediT authorship contribution statement

Wei Jiang: Writing – review & editing, Writing – original draft, Supervision, Investigation, Funding acquisition, Conceptualization. **Jian Zhou:** Writing – original draft, Investigation, Data curation. **Yang Cao:** Writing – review & editing, Supervision. **Ao Meng:** Methodology. **Runchang Liu:** Investigation, Data curation. **Jiansheng Li:** Visualization, Investigation. **Zhumin Li:** Investigation. **Yu Zhao:** Investigation. **Yonghao Zhao:** Writing – review & editing, Funding acquisition.

Declaration of competing interest

The authors declare that they have no known competing financial interests or personal relationships that could have appeared to influence the work reported in this paper.

Acknowledgements

The authors acknowledge financial supports from National Natural Science Foundation of China (Grant No. 52301124), the National Key R&D Program of China (Grant No. 2021YFA1200203), Anhui Provincial Natural Science Foundation (Grant No. 2308085QE131), and the Introduced Talent Scientific Research Launch Foundation of Anhui Polytechnic University (Grant No. 2023YQQ007).

References

[1] J.W. Yeh, S.K. Chen, S.J. Lin, J.Y. Gan, T.S. Chin, T.T. Shun, C.H. Tsau, S. Y. Chang, Nanostructured high-entropy alloys with multiple principal elements: novel alloy design concepts and outcomes, Adv. Eng. Mater. 6 (2004) 299–303.
[2] B. Cantor, I.T.H. Chang, P. Knight, A.J.B. Vincent, Microstructural development in equiatomic multicomponent alloys, Mater. Sci. Eng. A 375-377 (2004) 213–218.
[3] Y. Zhang, T.T. Zuo, Z. Tang, M.C. Gao, K.A. Dahmen, P.K. Liaw, Z.P. Lu, Microstructures and properties of high-entropy alloys, Prog. Mater. Sci. 61 (2014) 1–93.
[4] Y.Q. Wu, P.K. Liaw, R.X. Li, W.R. Zhang, G.H. Geng, X.H. Yan, G.Q. Liu, Y. Zhang, Relationship between the unique microstructures and behaviors of high-entropy alloys, Int. J. Miner. Metall. Mater. 31 (2024) 1350–1363.
[5] W. Jiang, S.Y. Yuan, Y. Cao, Y. Zhang, Y.H. Zhao, Mechanical properties and deformation mechanisms of a $Ni_2Co_1Fe_1V_{0.5}Mo_{0.2}$ medium-entropy alloy at elevated temperatures, Acta Mater. 213 (2021) 116982.
[6] Z.M. Li, K.G. Pradeep, Y. Deng, D. Raabe, C.C. Tasan, Metastable high-entropy dual-phase alloys overcome the strength-ductility trade-off, Nature 534 (2016) 227–230.
[7] B. Gludovatz, A. Hohenwarter, D. Catoor, E.H. Chang, E.P. George, R.O. Ritchie, A fracture-resistant high-entropy alloy for cryogenic applications, Science 345 (2014) 1153–1158.
[8] D.H. Cook, P. Kumar, M.I. Payne, C.H. Belcher, P. Borges, W.Q. Wang, F. Walsh, Z.H. Li, A. Devaraj, M.W. Zhang, M. Asta, A.M. Minor, E.J. Lavernia, D. Apelian, R.O. Ritchie, Kink bands promote exceptional fracture resistance in a NbTaTiHf refractory medium-entropy alloy, Science 384 (2024) 178–184.
[9] W. Jiang, Y. Cao, S.Y. Yuan, Y. Zhang, Y.H. Zhao, Creep properties and deformation mechanisms of a $Ni_2Co_1Fe_1V_{0.5}Mo_{0.2}$ medium-entropy alloy, Acta Mater. 245 (2023) 118590.

[10] T.K. Tsao, A.C. Yeh, C.M. Kuo, K. Kakehi, H. Murakami, J.W. Yeh, S.R. Jian, The high temperature tensile and creep behaviors of high entropy superalloy, Sci. Rep. 7 (2017) 12658.

[11] X.Z. Gao, Y.P. Lu, J.Z. Liu, J. Wang, T.M. Wang, Y.H. Zhao, Extraordinary ductility and strain hardening of $Cr_{26}Mn_{20}Fe_{20}Co_{20}Ni_{14}$ TWIP high-entropy alloy by cooperative planar slipping and twinning, Materialia 8 (2019) 100485.

[12] B.W. Xu, H.C. Duan, X.F. Chen, J. Wang, Y. Ma, P. Jiang, F.P. Yuan, Y.D. Wang, Y. Ren, K. Du, Y.G. Wei, X.L. Wu, Harnessing instability for work hardening in multi-principal element alloys, Nat. Mater. 23 (2024) 755–761.

[13] S.C. Lim, Recent developments in wear-mechanism maps, Tribol. Int. 31 (1998) 87–97.

[14] J. Joseph, N. Haghdadi, K. Shamlaye, P. Hodgson, M. Barnett, D. Fabijanic, The sliding wear behaviour of CoCrFeMnNi and Al_xCoCrFeNi high entropy alloys at elevated temperatures, Wear 428-429 (2019) 32–44.

[15] C. Nagarjuna, H.J. You, S. Ahn, J.W. Song, K.Y. Jeong, B. Madavali, G. Song, Y. S. Na, J.W. Won, H.S. Kim, S.J. Hong, Worn surface and subsurface layer structure formation behavior on wear mechanism of CoCrFeMnNi high entropy alloy in different sliding conditions, Appl. Surf. Sci. 549 (2021) 149202.

[16] J.W. Miao, T.M. Guo, J.F. Ren, A.J. Zhang, B. Su, J.H. Meng, Optimization of mechanical and tribological properties of FCC CrCoNi multi-principal element alloy with Mo addition, Vacuum 149 (2018) 324–330.

[17] Y.S. Geng, J. Chen, H. Tan, J. Cheng, J. Yang, W.M. Liu, Vacuum tribological behaviors of CoCrFeNi high entropy alloy at elevated temperatures, Wear 456-457 (2020) 203368.

[18] L. Yang, Z. Cheng, W.W. Zhu, C.C. Zhao, F.Z. Ren, Significant reduction in friction and wear of a high-entropy alloy via the formation of self-organized nanolayered structure, J. Mater. Sci. Technol. 73 (2021) 1–8.

[19] X. Chen, Z. Han, X.Y. Li, K. Lu, Lowering coefficient of friction in Cu alloys with stable gradient nanostructures, Sci. Adv. 2 (2016) e1601942.

[20] J.Y. He, S.K. Makineni, W.J. Lu, Y. Shang, Z.P. Lu, Z.M. Li, B. Gault, On the formation of hierarchical microstructure in a Mo-doped NiCoCr medium-entropy alloy with enhanced strength-ductility synergy, Scr. Mater. 175 (2020) 1–6.

[21] R.B. Chang, W. Fang, X. Bai, C.Q. Xia, X. Zhang, H.Y. Yu, B.X. Liu, F.X. Yin, Effects of tungsten additions on the microstructure and mechanical properties of CoCrNi medium entropy alloys, J. Alloys Compd. 790 (2019) 732–743.

[22] W.J. Lu, X. Luo, Y.Q. Yang, J.T. Zhang, B. Huang, Effects of Al addition on structural evolution and mechanical properties of the CrCoNi medium-entropy alloy, Mater. Chem. Phys. 238 (2019) 121841.

[23] W.H. Liu, J.Y. He, H.L. Huang, H. Wang, Z.P. Lu, C.T. Liu, Effects of Nb additions on the microstructure and mechanical property of CoCrFeNi high-entropy alloys, Intermetallics 60 (2015) 1–8.

[24] Y.L. Liu, F. Zhang, Z.Y. Huang, Q. Zhou, Y. Ren, Y. Du, H.F. Wang, Mechanical and dry sliding tribological properties of CoCrNiNbx medium-entropy alloys at room temperature, Tribol. Int. 163 (2021) 107160.

[25] V. Bhardwaj, Q. Zhou, F. Zhang, W.C. Han, Y. Du, K. Hua, H.F. Wang, Effect of Al addition on the microstructure, mechanical and wear properties of TiZrNbHf refractory high entropy alloys, Tribol. Int. 160 (2021) 107031.

[26] Y.P. Lu, Y. Dong, S. Guo, L. Jiang, H.J. Kang, T.M. Wang, B. Wen, Z.J. Wang, J. C. Jie, Z.Q. Cao, H.H. Ruan, T.L. Li, A promising new class of high-temperature alloys: eutectic high-entropy alloys, Sci. Rep. 4 (2014) 6200.

[27] X.Z. Gao, Y.P. Lu, B. Zhang, N.N. Liang, G.Z. Wu, G. Sha, J.Z. Liu, Y.H. Zhao, Microstructural origins of high strength and high ductility in an $AlCoCrFeNi_{2.1}$ eutectic high-entropy alloy, Acta Mater. 141 (2017) 59–66.

[28] M.E. Glicksman, Principles Of Solidification: An Introduction To Modern Casting And Crystal Growth Concepts, Springer Verlag, New York, 2010.

[29] Y.T. Zhu, X.L. Wu, Perspective on hetero-deformation induced (HDI) hardening and back stress, Mater. Res. Lett. 7 (2019) 393–398.

[30] Y. Liu, M.N. Xu, L.R. Xiao, X.F. Chen, Z.H. Hu, B. Gao, N.N. Liang, Y.T. Zhu, Y. Cao, H. Zhou, Dislocation array reflection enhances strain hardening of a dual-phase heterostructured high-entropy alloy, Mater. Res. Lett. 11 (2023) 638–647.

[31] S. Wang, Y.J. Xu, Z.G. Yu, H. Tan, S.M. Du, Y.Z. Zhang, J. Yang, W.M. Liu, Synthesis, microstructure and mechanical properties of a MoAlB ceramic prepared by spark plasma sintering from elemental powders, Ceram. Int. 45 (2019) 23515–23521.

[32] M. Naveed, A.F. Renteria, D. Nebel, S. Weiß, Study of high velocity solid particle erosion behaviour of Ti2AlC MAX phase coatings, Wear 342-343 (2015) 391–397.

[33] S. Gupta, M.W. Barsoum, On the tribology of the MAX phases and their composites during dry sliding: a review, Wear 271 (9) (2011) 1878–1894.

[34] X.D. Sui, J.Y. Liu, S.T. Zhang, J. Yang, J.Y. Hao, Microstructure, mechanical and tribological characterization of CrN/DLC/Cr-DLC multilayer coating with improved adhesive wear resistance, Appl. Surf. Sci. 439 (2018) 24–32.

[35] Q. Zhou, Y. Du, Y. Ren, W.W. Kuang, W.C. Han, H.F. Wang, P. Huang, F. Wang, J. Wang, Investigation into nanoscratching mechanical performance of metallic glass multilayers with improved nano-tribological properties, J. Alloys Compd. 776 (2019) 447–459.

[36] J.W. Miao, H. Liang, A.J. Zhang, J.Y. He, J.H. Meng, Y.P. Lu, Tribological behavior of an $AlCoCrFeNi_{2.1}$ eutectic high entropy alloy sliding against different counterfaces, Tribol. Int. 153 (2021) 106599.

[37] T.D. Vo, B. Tran, A.K. Tieu, D. Wexler, G. Deng, C. Nguyen, Effects of oxidation on friction and wear properties of eutectic high-entropy alloy $AlCoCrFeNi_{2.1}$, Tribol. Int. 160 (2021) 107017.

[38] Y.S. Geng, H. Tan, L. Wang, A.K. Tieu, J. Chen, J. Cheng, J. Yang, Nano-coupled heterostructure induced excellent mechanical and tribological properties in AlCoCrFeNi high entropy alloy, Tribol. Int. 154 (2021) 106662.

[39] C. Nguyen, A.K. Tieu, G.Y. Deng, D. Wexler, B. Tran, T.D. Vo, Study of wear and friction properties of a Co-free $CrFeNiAl_{0.4}Ti_{0.2}$ high entropy alloy from 600 to 950°C, Tribol. Int. 169 (2022) 107453.

[40] J.F. Archard, Contact and rubbing of flat surfaces, J. Appl. Phys. 24 (1953) 981–988.

[41] L.M. Du, L.W. Lan, S. Zhu, H.J. Yang, X.H. Shi, P.K. Liaw, J.W. Qiao, Effects of temperature on the tribological behavior of $Al_{0.25}$CoCrFeNi high-entropy alloy, J. Mater. Sci. Technol. 35 (2019) 917–925.

[42] A. Meng, F. Liang, Q.Z. Mao, Y. Fan, Y. Lin, X. Chen, Y.H. Zhao, Tribo-induced microstructural changes and associated wear mechanisms of $CoFeNi_2$ medium entropy alloy at elevated temperatures, Tribol. Int. 189 (2023) 108892.

[43] J.M. Wu, S.J. Lin, J.W. Yeh, S.K. Chen, Y.S. Huang, H.C. Chen, Adhesive wear behavior of AlxCoCrCuFeNi high-entropy alloys as a function of aluminum content, Wear 261 (2006) 513–519.

[44] A. Ayyagari, C. Barthelemy, B. Gwalani, R. Banerjee, T.W. Scharf, S. Mukherjee, Reciprocating sliding wear behavior of high entropy alloys in dry and marine environments, Mater. Chem. Phys. 210 (2018) 162–169.

[45] G.Y. Deng, A.K. Tieu, L.H. Su, P. Wang, L. Wang, X.D. Lan, S.G. Cui, H.T. Zhu, Investigation into reciprocating dry sliding friction and wear properties of bulk CoCrFeNiMo high entropy alloys fabricated by spark plasma sintering and subsequent cold rolling processes: role of Mo element concentration, Wear 460-461 (2020) 203440.

[46] Y. Yu, F. He, Z.H. Qiao, Z.J. Wang, W.M. Liu, J. Yang, Effects of temperature and microstructure on the triblogical properties of CoCrFeNiNbx eutectic high entropy alloys, J. Alloys Compd. 775 (2019) 1376–1385.

[47] M. Chen, L.W. Lan, X.H. Shi, H.J. Yang, M. Zhang, J.W. Qiao, The tribological properties of $Al_{0.6}$CoCrFeNi high-entropy alloy with the σ phase precipitation at elevated temperature, J. Alloys Compd. 777 (2019) 180–189.

[48] M. Chen, X.H. Shi, H.J. Yang, P.K. Liaw, M.C. Gao, J.A. Hawk, J.W. Qiao, Wear behavior of $Al_{0.6}$CoCrFeNi high-entropy alloys: effect of environments, J. Mater. Res. 33 (2018) 3310–3320.

[49] H. Cheng, Y.H. Fang, J.M. Xu, C.D. Zhu, P.Q. Dai, S.X. Xue, Tribological properties of nano/ultrafine-grained FeCoCrNiMnAlx high-entropy alloys over a wide range of temperatures, J. Alloys Compd. 817 (2020) 153305.

[50] B. Gwalani, A.V. Ayyagari, D. Choudhuri, T. Scharf, S. Mukherjee, M. Gibson, R. Banerjee, Microstructure and wear resistance of an intermetallic-based $Al_{0.25}Ti_{0.75}$CoCrFeNi high entropy alloy, Mater. Chem. Phys. 210 (2018) 197–206.

[51] C. Huang, Y.Z. Zhang, R. Vilar, J.Y. Shen, Dry sliding wear behavior of laser clad TiVCrAlSi high entropy alloy coatings on Ti–6Al–4V substrate, Mater. Des. 41 (2012) 338–343.

[52] Y. Liu, S.G. Ma, M.C. Gao, C. Zhang, T. Zhang, H.J. Yang, Z.H. Wang, J.W. Qiao, Tribological properties of $AlCrCuFeNi_2$ high-entropy alloy in different conditions, Metall. Mater. Trans. A 47 (2016) 3312–3321.

[53] S. Pan, C.C. Zhao, P.B. Wei, F.Z. Ren, Sliding wear of CoCrNi medium-entropy alloy at elevated temperatures: wear mechanism transition and subsurface microstructure evolution, Wear 440-441 (2019) 203108.

[54] Y.X. Wang, Y.J. Yang, H.J. Yang, M. Zhang, S.G. Ma, J.W. Qiao, Microstructure and wear properties of nitrided AlCoCrFeNi high-entropy alloy, Mater. Chem. Phys. 210 (2018) 233–239.

[55] Y.X. Wang, Y.J. Yang, H.J. Yang, M. Zhang, J.W. Qiao, Effect of nitriding on the tribological properties of $Al_{1.3}CoCuFeNi_2$ high-entropy alloy, J. Alloys Compd. 725 (2017) 365–372.

[56] A.J. Zhang, J.S. Han, B. Su, P.D. Li, J.S. Meng, Microstructure, mechanical properties and tribological performance of CoCrFeNi high entropy alloy matrix self-lubricating composite, Mater. Des. 114 (2017) 253–263.

[57] A.J. Zhang, J.S. Han, B. Su, J.H. Meng, A novel CoCrFeNi high entropy alloy matrix self-lubricating composite, J. Alloys Compd. 725 (2017) 700–710.

[58] A.J. Zhang, J.S. Han, B. Su, J.H. Meng, A promising new high temperature self-lubricating material: $CoCrFeNiS_{0.5}$ high entropy alloy, Mater. Sci. Eng.A 731 (2018) 36–43.

[59] A. Leyland, A. Matthews, On the significance of the H/E ratio in wear control: a nanocomposite coating approach to optimised tribological behaviour, Wear 246 (2000) 1–11.

[60] M. Zhang, X.H. Zhang, M.Y. Niu, Z.S. Jiang, H. Chen, Y.H. Sun, High-temperature tribological behavior of CoCrFeNiV high-entropy alloys: a parallel comparison with CoCrFeNiMn high-entropy alloys, Tribol. Int. 174 (2022) 107736.

[61] G.B. Tang, J.F. Yang, Z.B. Huang, J.H. Li, M.L. Yang, H.B. Hu, Z.W. Liang, Grain refinement of CoCrFeNiMn high-entropy alloy for improved high-temperature tribological properties, J. Alloys Compd. 1014 (2025) 178853.

[62] G.P. Lin, Z.B. Cai, Y.H. Dong, B.X. Wang, C.M. Wang, Z. Liu, P. Zhang, L. Gu, Mechanical properties and tribological behavior of Al0.5CoCrFeNb0.5Ni high-entropy alloy at high temperatures, J. Mater. Res. Technol. 30 (2024) 8718–8730.

[63] Z.P. Sun, X.Y. Zhang, X.Z. Li, Z.M. Xu, C. Li, Z.M. Wang, Study on the wear behavior of $CoCrFeNiAl_{1.0}$ high entropy alloy at high temperature, Mater. Lett. 324 (2022) 132726.

[64] T.W. Xu, J.Y. Li, Y. Yu, T.Y. Li, L.J. Wang, H.G. Tang, Z.H. Qiao, High-temperature tribological properties of $Fe_{50}Mn_{25}Cr_5Al_{15}Ti_5$ iron-based high-entropy alloys, Tribol. Int 204 (2025) 110423.

[65] Y.S. Geng, H. Tan, J. Cheng, J. Chen, Q.C. Sun, S.Y. Zhu, J. Yang, Microstructure, mechanical and vacuum high temperature tribological properties of AlCoCrFeNi high entropy alloy based solid-lubricating composites, Tribol. Int. 151 (2020) 106444.

[66] Q. Wan, K. Hua, Z.Q. Zhou, F. Zhang, H.X. Wu, Q. Zhou, H.F. Wang, Revealing the B addition on tribology performance in $TiZrHfTa_{0.5}$ refractory high-entropy alloy at ambient and elevated temperature, J. Alloys Compd. 931 (2023) 167521.

[67] G.Y. Deng, B.S. Dong, C. Zhang, R. Wang, Z. Yang, N. Nie, P. Wang, L. Wang, H. Wang, Y.Z. Tian, L.H. Su, H.J. Li, Microstructure, microhardness and high-temperature tribological properties of $CoCrFeNiMnTi_{0.3}$ high entropy alloy coating manufactured by powder-bed arc additive manufacturing, Surf. Coat. Technol. 485 (2024) 130918.

[68] D. Chen, X.F. Cui, Y.J. Guan, X.Y. Li, S. Ma, Z.T. Dai, Z.Y. Song, L.T. Feng, G. Jin, J.N. Liu, Study on enhanced wear resistance of FeCoCrNi2MoSi high entropy alloy coatings induced by nano-layered eutectic and laves phase, Tribol. Int. 194 (2024) 109534.

[69] Q. Zhou, Z.C. Jiao, Z.B. Huang, Y.R. Shi, Y.L. Li, C.H. Yin, H.F. Wang, H.C. Pinto, C. Greiner, W.M. Liu, Wear-resistant CrCoNi nanocrystalline film via friction-driven surface segregation, Acta Mater. 279 (2024) 120299.

[70] H. Wang, D.K. Chen, X.H. An, Y. Zhang, S.J. Sun, Y.Z. Tian, Z.F. Zhang, A. G. Wang, J.Q. Liu, M. Song, S.P. Ringer, T. Zhu, X.Z. Liao, Deformation-induced crystalline-to-amorphous phase transformation in a CrMnFeCoNi high-entropy alloy, Sci. Adv. 7 (2021) eabe3105.

[71] Y. Cao, L.C. Zhang, Y. Zhang, Twinning interactions induced amorphisation in ultrafine silicon grains, Mater. Sci. Eng.A 658 (2016) 321–325.

[72] I.S. Wani, T. Bhattacharjee, S. Sheikh, Y.P. Lu, S. Chatterjee, P.P. Bhattacharjee, S. Guo, N. Tsuji, Ultrafine-grained $AlCoCrFeNi_{2.1}$ eutectic high-entropy alloy, Mater. Res. Lett. 4 (2016) 174–179.

[73] A. Lozinko, R. Gholizadeh, Y.B. Zhang, U. Klement, N. Tsuji, O.V. Mishin, S. Guo, Evolution of microstructure and mechanical properties during annealing of heavily rolled $AlCoCrFeNi_{2.1}$ eutectic high-entropy alloy, Mater. Sci. Eng.A 833 (2022) 142558.

[74] I.S. Wani, T. Bhattacharjee, S. Sheikh, P.P. Bhattacharjee, S. Guo, N. Tsuji, Tailoring nanostructures and mechanical properties of $AlCoCrFeNi_{2.1}$ eutectic high entropy alloy using thermo-mechanical processing, Mater. Sci. Eng.A 675 (2016) 99–109.

[75] F. Popa, I. Chicinas, O. Isnard, AlSb intermetallic semiconductor compound formation by solid state reaction after partial amorphization induced by mechanical alloying, Intermetallics 93 (2018) 371–376.

[76] C.H. Yin, Y.L. Liang, Y. Liang, W. Li, M. Yang, Formation of a self-lubricating layer by oxidation and solid-state amorphization of nano-lamellar microstructures during dry sliding wear tests, Acta Mater. 166 (2019) 208–220.

[77] S.Y. Tarassov, A.V. Kolubaev, Effect of friction on subsurface layer microstructure in austenitic and martensitic steels, Wear 231 (1999) 228–234.

[78] S. Zhao, B. Kad, E.N. Hahn, B.A. Remington, C.E. Wehrenberg, C.M. Huntington, H.S. Park, E.M. Bringa, K.L. More, M.A. Meyers, Pressure and shear-induced amorphization of silicon, Extreme Mech. Lett. 5 (2015) 74–80.

[79] Z.S. Fan, H.P. Yu, C.F. Li, Interface and grain-boundary amorphization in the Al/Fe bimetallic system during pulsed-magnetic-driven impact, Scr. Mater. 110 (2016) 14–18.

[80] S.T. Zhao, Z.Z. Li, C.Y. Zhu, W. Yang, Z.R. Zhang, D.E.J. Armstrong, P.S. Grant, R. O. Ritchie, M.A. Meyers, Amorphization in extreme deformation of the CrMnFeCoNi high-entropy alloy, Sci. Adv. 7 (2021) eabb3108.

[81] Y.H. Zhao, Thermodynamic model for solid-state amorphization of pure elements by mechanical-milling, J. Non-Cryst. Solids 352 (2006) 5578–5585.

[82] M.R. Jones, B.L. Nation, J.A. Wellington-Johnson, J.F. Curry, A.B. Kustas, P. Lu, M. Chandross, N. Argibay, Evidence of inverse Hall-Petch behavior and low friction and wear in high entropy alloys, Sci. Rep. 10 (2020) 10151.

[83] X. Wang, X.C. Wei, X.L. Hong, J.Y. Yang, W.R. Wang, Formation of sliding friction-induced deformation layer with nanocrystalline structure in T10 steel against 20CrMnTi steel, Appl. Surf. Sci. 280 (2013) 381–387.

[84] H. Kato, M. Sasase, N. Suiya, Friction-induced ultra-fine and nanocrystalline structures on metal surfaces in dry sliding, Tribol. Int. 43 (2010) 925–928.

[85] L.L. Wang, Y. Cao, Y.H. Zhao, Lattice distortion promotes incipient plasticity in multiprincipal element alloys, Nano Lett. 24 (2024) 9004–9010.

[86] J.S. Li, J. Zhou, Y.F. Liu, K. Wei, J.F. Liu, Y.C. Xi, Z.M. Li, T. Liu, W. Jiang, Microstructural origins of impact resistance of $AlCoCrFeNi_{2.1}$ eutectic high-entropy alloy, Mater. Sci. Eng.A 890 (2024) 145921.

[87] Y. Cao, S. Ni, X.Z. Liao, M. Song, Y.T. Zhu, Structural evolutions of metallic materials processed by severe plastic deformation, Mater. Sci. Eng.R 133 (2018) 1–59.

[88] W.J. Kuang, M. Song, G.S. Was, Insights into the stress corrosion cracking of solution annealed alloy 690 in simulated pressurized water reactor primary water under dynamic straining, Acta Mater. 151 (2018) 321–333.

[89] C. Liu, Z.M. Li, W.J. Lu, Y. Bao, W.Z. Xia, X.X. Wu, H. Zhao, B. Gault, C.L. Liu, M. Herbig, A. Fischer, G. Dehm, G. Wu, D. Raabe, Reactive wear protection through strong and deformable oxide nanocomposite surfaces, Nat. Commun. 12 (2021) 5518.

[90] A. Meng, F. Liang, L. Gu, Q.Z. Mao, Y.P. Zhang, X. Chen, Y.H. Zhao, An exceptionally wear-resistant $CoFeNi_2$ medium entropy alloy via tribo-induced nanocrystallites with amorphous boundaries, Appl. Surf. Sci. 614 (2023) 156102.

[91] A. Takeuchi, A. Inoue, Classification of bulk metallic glasses by atomic size difference, heat of mixing and period of constituent elements and its application to characterization of the main alloying element, Mater. Trans. 46 (2005) 2817–2829.

[92] Y. Matsukawa, S. Kitayama, K. Murakami, Y. Shinohara, K. Yoshida, H. Maeno, H. L. Yang, T. Toyama, K. Yasuda, H. Watanabe, A. Kimura, H. Muta, S. Yamanaka, Y.F. Li, Y. Satoh, S. Kano, H. Abe, Reassessment of oxidation-induced amorphization and dissolution of Nb precipitates in Zr−Nb nuclear fuel cladding tubes, Acta Mater. 127 (2017) 153–164.

[93] J.B. Zhao, B. Li, W.M. Huang, Y.X. Wang, J.L. Han, X. Wang, High-temperature rheological behavior and composition design of Hf-Be-Ti-Zr-Cu-Ni High-entropy amorphous alloy, Trans. Indian Inst. Met. 76 (2023) 1165–1174.

[94] G.Y. Deng, A.K. Tieu, X.D. Lan, L.H. Su, L. Wang, Q. Zhu, H.T. Zhu, Effects of normal load and velocity on the dry sliding tribological behaviour of $CoCrFeNiMo_{0.2}$ high entropy alloy, Tribol. Int. 144 (2020) 106116.

[95] N. Hashemi, A. Mertens, H.M. Montrieux, J.T. Tchuindjang, O. Dedry, R. Carrus, J. Lecomte-Beckers, Oxidative wear behaviour of laser clad high speed steel thick deposits: influence of sliding speed, carbide type and morphology, Surf. Coat. Technol. 315 (2017) 519–529.

[96] D.N. Hanlon, W.M. Rainforth, The rolling sliding wear response of conventionally processed and spray formed high speed steel at ambient and elevated temperature, Wear 255 (2003) 956–966.

[97] A. Pauschitz, M. Roy, F. Franek, Mechanisms of sliding wear of metals and alloys at elevated temperatures, Tribol. Int. 41 (2008) 584–602.

[98] J. Cheng, F. Li, S.Y. Zhu, J.Y. Hao, J. Yang, W.S. Li, W.M. Liu, High temperature tribological properties of a nickel-alloy-based solid-lubricating composite: effect of surface tribo-chemistry, counterpart and mechanical properties, Wear 386-387 (2017) 39–48.

[99] X.X. Li, Y. Zhou, X.L. Ji, Y.X. Li, S.Q. Wang, Effects of sliding velocity on tribo-oxides and wear behavior of Ti–6Al–4V alloy, Tribol. Int. 91 (2015) 228–234.

[100] H. So, D.S. Yu, C.Y. Chuang, Formation and wear mechanism of tribo-oxides and the regime of oxidational wear of steel, Wear 253 (2002) 1004–1015.

[101] M.D. Demetriou, M.E. Launey, G. Garrett, J.P. Schramm, D.C. Hofmann, W. L. Johnson, R.O. Ritchie, A damage-tolerant glass, Nat. Mater. 10 (2011) 123–128.

[102] Y.B. Wang, D.D. Qu, X.H. Wang, Y. Cao, X.Z. Liao, M. Kawasaki, S.P. Ringer, Z. W. Shan, T.G. Langdon, J. Shen, Introducing a strain-hardening capability to improve the ductility of bulk metallic glasses via severe plastic deformation, Acta Mater. 60 (2012) 253–260.

[103] A.L. Greer, Metallic glasses, Science 267 (1995) 1947–1953.

[104] D. Jang, J.R. Greer, Transition from a strong-yet-brittle to a stronger-and-ductile state by size reduction of metallic glasses, Nat. Mater. 9 (2010) 215–219.

[105] G. Wu, S. Balachandran, B. Gault, W.Z. Xia, C. Liu, Z.Y. Rao, Y. Wei, S.F. Liu, J. Lu, M. Herbig, W.J. Lu, G. Dehm, Z.M. Li, D. Raabe, Crystal–glass high-entropy nanocomposites with near theoretical compressive strength and large deformability, Adv. Mater. 32 (2020) 2002619.